

Determination of the
Spectroscopic Quadrupole
moment of the first 2^+ excited
state in ^{32}S

Lihleli Mavela



UNIVERSITY *of the*
WESTERN CAPE

A thesis is submitted in fulfillment of the requirements
of the Masters in Science degree in the Department of
Physics and Astronomy, University of the Western
Cape.

supervised by:

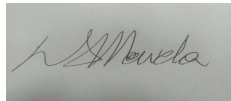
Prof. J. N. Orce, University of the Western Cape.

May 2, 2019

Declaration

I declare that *Determination of the spectroscopic quadrupole moment of the first 2^+ excited state in ^{32}S* is my own work, that it has not been submitted for any degree or examination in any other university, and that all sources I have used or quoted have been indicated and acknowledged by complete references.

Full name: Lihleli Mavela



Signed :



Abstract

In this work we have determined the spectroscopic or static quadrupole moment of the first excited state ($Q_s(2_1^+)$) lying at 2230.6 keV in ^{32}S using the reorientation effect. The Coulomb-excitation experiment at safe bombarding energies was performed at iThemba LABS's AFRODITE vault, where ^{32}S beams at 120.3 MeV were bombarded onto a ^{194}Pt target of 1 mg/cm^2 thickness. The beam energy has been chosen such that the separation between nuclear surfaces is greater than 6.5 fm at all scattering angles, in order to avoid nuclear interactions. A double-sided CD-type S3 silicon detector, with 24 rings and 32 sectors, has been placed upstream (at backward angles) to detect the scattered particles. Gamma rays have been detected with the AFRODITE clover array. This particle-gamma coincidence experiment allows for an angular distribution and Doppler correction of the gamma rays emitted at 9% the speed of light. The cross sections (or gamma-ray integrated yields) measured as a function of scattering angle θ at backward angles are sensitive to second-order perturbation effects in Coulomb excitation, i.e., diagonal matrix elements which are directly related to the spectroscopic quadrupole moment. The gamma-ray integrated yields obtained from this experiment are compared with the GOSIA simulations, yielding a new measurement of $Q_s(2_1^+) = -0.10 \pm 0.7\text{ eb}$, which corresponds to a prolate shape in the intrinsic frame of the nucleus. The uncertainty of this measurement is limited by statistics. This result agrees with previous measurements and confirms the zig zag of shapes at the end of the *sd* shell when approaching the doubly-magic nucleus ^{40}Ca . Nonetheless, the mystery continues as a prolate shape for the first 2^+ disagrees with modern theoretical mean-field calculations and the pairing coupling model.

Acknowledgements

I would like to cordially give appreciation to the following people:

- The God I serve for the opportunity and grace He gave me to do my MSc.
- My parents, Nokwandisa (Kwandi) and Mzwamanda (Ta Mzala) Ngwabeni, for the love and support they gave me before and during my studies.
- My supervisor, Prof. Nico Orce, for allowing me to do my MSc degree with him, for the training and support he offered and the patience he had with me.
- George O'Neil, Kushal Kapoor, Paul Garret and Tshepo Dinoko for their assistance on my thesis writing.
- Makabata Mokgolobotho and Craig Mehl for their assistance on the data sorting.
- The entire UWC Coulex group for their warm friendship and spirit of UBUNTU they uphold.
- The iThemba LABS AFRODITE group and other individuals who took shifts during my experiment.
- Magda Zielinska for her time and patience to walk me through GOSIA calculations.
- Last but not least my two brothers and friends, Songeziwe Ntsimango and Sondisa Mxotwa, for their greatest support and encouragement.



UNIVERSITY of the
WESTERN CAPE

Contents

1	Introduction	1
1.1	Scientific Motivation	4
2	Theoretical Review	8
2.1	Coulomb Excitation	8
2.2	Safe Coulomb Excitation	8
2.2.1	Coulomb Barrier	8
2.2.2	Distance between nuclear surfaces	10
2.3	Semi-classical Approximation	10
2.3.1	Sommerfeld Parameter η	11
2.3.2	Adiabaticity Parameter ξ	12
2.4	Coulomb Excitation Cross-sections	12
2.4.1	Rutherford scattering cross-sections	13
2.4.2	First-order Coulomb Excitation	13
2.4.3	Second-Order Coulomb Excitation	14
2.5	Nuclear Models	16
2.5.1	Shell Model	17
2.6	Collective Model	21
2.6.1	Rotational States	21
2.6.2	Vibrational States	22
3	Experimental Details	24
3.1	Experimental Design	24
3.1.1	“Safe” Beam Energy	24
3.1.2	Semi-Classical Approximation	25
3.2	Particle and Gamma ray Detection	26
3.3	Gamma-ray Detection	27
3.4	AFRODITE	27
3.4.1	Clover Detector	29
3.4.2	S3 Silicon Detector	31
3.5	Electronics and Data Acquisition System	32
4	Analysis and Results	34
4.1	Calibration	34
4.1.1	Efficiency Calibration	34
4.1.2	HPGe Clover Detector Energy Calibration	36
4.1.3	Silicon Detector Energy Calibration and Particle Energy Loss	36

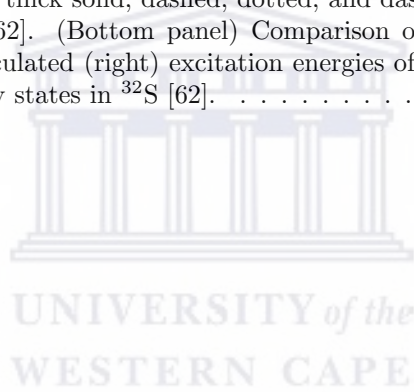
4.2	Background Radiation	38
4.2.1	Broad Particle Energy Gate	38
4.2.2	Particle Coincidence	39
4.2.3	Particle- γ Coincidence	40
4.2.4	Energy Difference and Inelastic Conditions	41
4.3	Doppler Corrections	42
4.3.1	Background Subtraction and Doppler Corrections	44
4.4	GOSIA code and determination of $Q_S(2_1^+)$	48
5	Discussion and Conclusions	52
5.1	Discussion	52
5.2	Conclusion	54
A	AFRODITE detector angles	55
A.1	AFRODITE clover angle	55
A.2	Clover crystal angles	56
B	S3 Silicon detector dimensions	57
B.1	S3 Silicon Detector ring radii and average scattering angles	58
C	Sorting Code	59
D	GOSIA input	68



List of Figures

1.1	Quadrupole shapes of the nucleus: $Q_0 < 0$ for oblate (left) and $Q_0 > 0$ for prolate (right) [10].	3
1.2	Adopted $Q_S(2_1^+)$ values as a function of A in the $2s - 1d$ shell from Spear's 1981 evaluation [11].	4
1.3	$ Q_S^{rot}(2_1^+) $ values of the $2s - 1d$ shell nuclei [11]	5
1.4	Energy spectra for the $^{208}\text{Pb}(^{32}\text{S}, ^{32}\text{S}^*)^{208}\text{Pb}^*$ reaction at different angles [17].	6
1.5	Previous measurements of $Q_S(2_1^+)$ values in ^{32}S plotted as a function of published year [11].	7
2.1	Example of Coulomb barrier as a function of the distance between the center of two nuclei.	9
2.2	Semi-classical approximation where the scattered particle follows a classical hyperbolic trajectory. [28]	11
2.3	The orientation of the magnetic substates is affected by a prolate shape.	16
2.4	Binding energy per nucleon B/A as a function of mass number A [36].	17
2.5	$S(2n)$ separation energy as a function of neutron number N [37].	18
2.6	Energy levels produced by the quantum harmonic oscillator [39].	19
2.7	Effects of spin-orbit interaction on quantum harmonic oscillator potential energy levels [39].	20
2.8	Lowest modes of vibration.	22
3.1	Showing the distance between nuclear surfaces as a function of laboratory scattering angles for 120.3 MeV beam energy.	25
3.2	The adiabaticity parameter as function of center-of-mass angles.	26
3.3	ARODITE Array.	28
3.4	Target Chamber.	29
3.5	Schematic representation of the HYGe clover crystals [55].	30
3.6	A typical Clover detector	30
3.7	S3 Silicon detector inside the target chamber	31
3.8	Schematic drawing of S3 silicon detector[56]	32
3.9	Sketch of the electronics setup for Coulomb-excitation experiments at iThemba LABS [56].	33
4.1	^{152}Eu calibration spectrum.	35
4.2	^{56}Co calibration spectrum.	36

4.3	Relative efficiency curve.	37
4.4	All clover spectrum overlapped after calibration.	38
4.5	First eight uncalibrated rings.	39
4.6	First twelve calibrated rings	40
4.7	Broad particle energy gating.	41
4.8	Time gates between adjacent rings and sectors.	42
4.9	Particle- γ time condition.	43
4.11	Spherical coordinates schematics.	44
4.12	Background radiation from the Doppler shifted spectra.	45
4.13	Background radiation from the Doppler corrected spectra.	45
4.14	Doppler shifted spectra with background radiation.	46
4.15	Doppler corrected spectra with background radiation.	46
4.16	Doppler shifted spectra with background radiation subtracted.	47
4.17	Doppler corrected spectra with background radiation subtracted.	47
4.19	$\langle 2_1^+ E2 2_1^+ \rangle - \langle 2_1^+ E2 0_1^+ \rangle$ plane.	49
4.20	$\langle 2_1^+ E2 2_1^+ \rangle - \langle 2_1^+ E2 0_1^+ \rangle$ plane with error bands.	50
5.1	(Top panel) Deformation energy curves for $J = 0, 2, 4,$ and 6 corresponding to thick solid, dashed, dotted, and dash-dotted lines, respectively [62]. (Bottom panel) Comparison of experimental (left) and calculated (right) excitation energies of even spin and positive parity states in ^{32}S [62].	53



List of Tables

2.1	A table of shell model calculations of Q_s and experimental values [41].	21
A.1	AFRODITE clover angles	55
A.2	AFRODITE crystal angles	56
B.1	S3 silicon detector ring radii	58



Chapter 1

Introduction

The nucleus is the positively-charged central core of an atom. It is made up of protons and neutrons, collectively known as nucleons. These nucleons are held together by the short-range strong nuclear forces. Due to the strong nuclear forces, when quantum mechanics is applied, discrete nuclear states are reproduced. These nuclear states are either ground or excited states. The ground state is the lowest state that a nucleus can have and is described by its nuclear binding energy, angular momentum and electromagnetic moment [1]. The energy of a nucleus in its ground state is calculated by the binding energy, the energy that holds the nucleons together[2],

$$B(Z, N) = [Zm_p + Nm_n - m(Z, N)]c^2, \quad (1.1)$$

where Z is the atomic number, N the number of neutrons, c the speed of light, m_p and m_n the mass of the protons and neutrons, respectively, and $B(Z, N)$ the binding energy of the nucleus with atomic number Z and number of neutrons equal to N . The binding energy gives the minimum energy needed to disassemble the nucleus and information about the stability of nuclei. It is also pivotal in beam energy (E_p) selection for the nuclear experiment of interest, since it will be an extreme to use E_p that is equal or greater than $B(Z, N)$. $B(Z, N)$ of ^{32}S is 271.78 MeV [3], while $E_p=120.3$ MeV was used in this present work. This implies that E_p will not disassemble the ^{32}S nucleus.

In contrast to the binding energy, the ground state is also described by the nuclear angular momentum. This is important in nuclear structure studies as it gives information about the motion of the nucleons. Total angular momentum or spin J of nuclear states are explained by quantum mechanics formalism and the shell model. Since J is explained by quantum mechanics, it is quantized in nature. In the shell model it is assumed that nucleons are independently moving in a spherical nucleus [4]. According to this model, nuclear shells and subshells present angular momentum quantum numbers that each nucleon can carry.

Since nucleons are fermions, this implies that they carry an intrinsic spin angular moment $s = \frac{1}{2}$ and the orbital angular moment ℓ which is an integer [5]. The coupling of s and ℓ gives a half-integer spin j for a single nucleon. The value of j is dictated by the fundamental property of nucleon pairing and by Pauli's exclusion principle. Pauli's exclusion principles states that fermions cannot have

the same quantum numbers at the same state. The two paired nucleons with the same orbital angular momentum will add up to $J = 0$ and the unpaired nucleon will have a half-integer spin. Shell model predicts that the spin of the ground state depends on the composition of nucleons in the shell. For even-odd nuclei J is equal to the angular momentum of the unpaired nucleon, for odd-odd nuclei J is equal to the integer and for an even-even nucleus $J = 0$ in its ground state [4].

Moreover, nuclear states are separated by the energy gaps. To excite a nucleus, a certain energy is needed to get it to a desired nuclear state. Shell model calculations predict more energy requirement to excite even-even nuclei [6]. The predicted energy is used in breaking the paired nucleon and excite at least one nucleon to the next state, which is separate from the ground state by a relatively large energy gap. However, some states are much closer, like the first 2_1^+ excited state. The 2_1^+ state is an important state because it provides evidence of the collectivity of a nucleus [2]. The collective model basically assumes that nucleons are a collective entity that moves as a whole body like a liquid drop. Further details on the shell and collective models will be discussed in Chapter 2.

A nucleus can be stable or radioactive. A stable nucleus is assumed to be in its ground state until it is excited, while a radioactive nucleus is any unstable nucleus that can give off any kind of radiation. An excited nucleus emits γ -ray radiation as it undergoes de-excitation. Excitation of the nucleus to a higher nuclear state is a process which may require external fields/potential [1]. The energy from the external potential will be added to a nucleus in order to gain sufficient energy to populate higher excited states. If the external potential is weak enough, then perturbation theory can be used to calculate the effects of the external potential [7].

In Coulomb excitation (CE), pure electromagnetic interactions are used as an external potential for nuclear excitation to populate the 2_1^+ states in ^{32}S and ^{196}Pt [8]. CE is an advantageous approach on perturbation theory due to the fact that electromagnetic theory is well known. As a result of perturbation theory approximations, reliable cross-sections can be calculated. More nuclear observables like reduced transition probabilities or $B(E2)$ values, spectroscopic quadrupole moments ($Q_s(J^\pi)$), and the nuclear polarizability can be extracted from reliable CE cross-sections. Using the advantages of CE and the recent state-of-the-art facilities for CE experiments, the $Q_s(2_1^+)$ value in ^{32}S can be reliably determined through the Coulomb-excitation reorientation effect (CERE). CERE is an effect which is characterized by second-order perturbation in Coulomb-excitation theory.

The $Q_s(J^\pi)$ value of a nuclear state with $J \neq 0$ or $1/2$ can be measured by the CERE [9] and provides the nuclear charge distribution with respect to the shape of a nucleus in the laboratory frame, which can be calculated as the expectation value of the electric quadrupole moment operator \hat{Q}_0 applied to the laboratory frame,

$$Q_s(J^\pi) = \langle J, M = J | \hat{Q}_0 | J, M = J \rangle, \quad (1.2)$$

$$Q_s(J^\pi) = \sqrt{\frac{J(2J-1)}{(2J+1)(2J+3)(J+1)}} \langle J || \hat{Q}_0 || J \rangle, \quad (1.2 \text{ a})$$

where J is the spin of the nuclear state, M the spin projection and

$$Q_0 = \int \rho(3z^2 - r^2)dV. \quad (1.2 \text{ b})$$

where Q_0 is the intrinsic quadrupole moment, ρ is the nuclear charge distribution, dV the differential nuclear volume and $r^2 = x^2 + y^2 + z^2$. According to equation 1.2 b, Q_0 can be defined as the deviation of a nuclear shape from the spherical shape, as shown in Fig. 1.1. Eq. 1.2 b also predicts that for $Q_0 > 0$ the nucleus will have a prolate shape, an oblate shape for $Q_0 < 0$ and a spherical shape for $Q_0 = 0$.

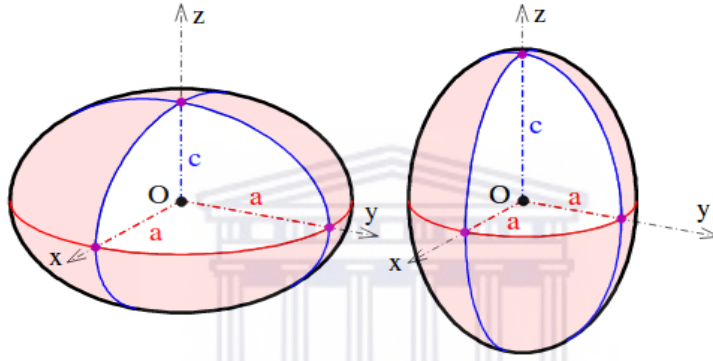


Figure 1.1: Quadrupole shapes of the nucleus: $Q_0 < 0$ for oblate (left) and $Q_0 > 0$ for prolate (right) [10].

Eq. 1.2 a suggests that nuclear states with spin $J = 1/2$ and $J = 0$ will have zero spectroscopic quadrupole moment, although these could have an intrinsic deformation Q_0 , which cannot be determined by the reorientation effect. Assuming that a nucleus is an ideal rotating ellipsoid with K being the projection of the total spin J onto the axis of symmetry, then $Q_s(J^\pi)$ and Q_0 are related by

$$Q_s(J^\pi) = \frac{3K^2 - J(J+1)}{(2J+3)(J+1)} Q_0. \quad (1.3)$$

For $J^\pi = 2^+$ and $K = 0$ (e.g. for the ground-state band), the spectroscopic quadrupole moment is given by,

$$Q_s(2^+) = -\frac{2}{7} Q_0. \quad (1.3 \text{ a})$$

for which $Q_s > 0$ will now yield an oblate-shaped nucleus, $Q_s < 0$ will yield a prolate-shaped nucleus and $Q_s = 0$ will still hold for a spherical nucleus. Since the nucleus is assumed to be a rotating ellipsoid, the adiabatic rotational model can relate spectroscopic quadrupole moments $|Q_s^{rot}(2^+)|$ to reduced $E2$ transition probabilities by the following equation [11],

$$|Q_s^{rot}(2^+)| = 0.9059 \sqrt{B(E2; 0^+ \rightarrow 2^+)}. \quad (1.4)$$

Evidently from Eq. 1.4, the measured $B(E2)$ values do not provide a sign for the $Q_s(2_1^+)$ value and can only be used to determine the magnitude of the deformation of a nucleus. $Q_s(J^\pi)$ is also predicted theoretically by different nuclear models. Using CE as the model-independent approach to accurately determine the $Q_s(2_1^+)$ value in ^{32}S will allow us to test the validity of modern nuclear models.

1.1 Scientific Motivation

Electric and magnetic moments have been used to understand the nuclear distribution of charges and currents. Different experimental probes can be used to measure nuclear moments, and the CERE has proven to be the most reliable and suitable for the determination of $Q_s(J^\pi)$ values [9].

About 160 stable even-even nuclei can be evaluated by CERE and about 40% have been studied. The nucleus ^{32}S with $A=32$ and $Z=16$ lies within the range $A=16-40$ of the $2s-1d$ shell. $Q_S(2_1^+)$ values in the $2s-1d$ region were evaluated by Spear *et al* in 1981 [11] and are shown in Fig. 1.2. Most of these $Q_S(2_1^+)$ values remain the adopted values in the National Nuclear Data Center (NNDC). Moreover, Fig. 1.3 shows the rotational-model values of $Q_S(2_1^+)$ calculated by Eq. 1.4, which illustrates clear deviations from the model-independent values provided by reorientation-effect measurements.

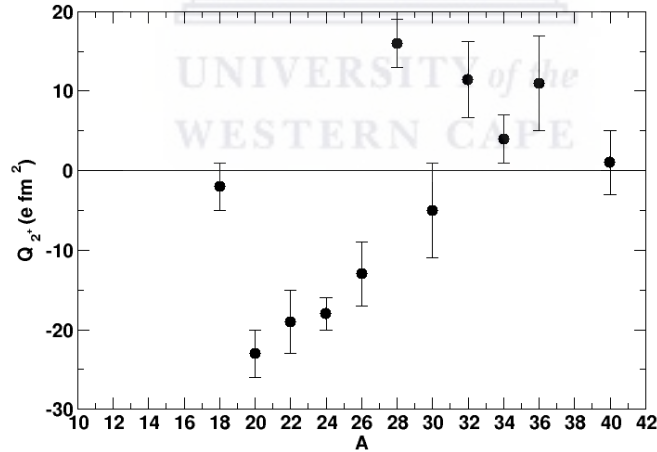


Figure 1.2: Adopted $Q_S(2_1^+)$ values as a function of A in the $2s-1d$ shell from Spear's 1981 evaluation [11].

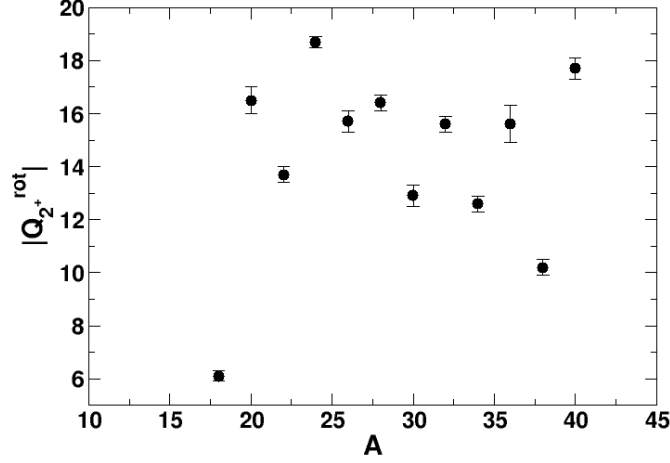


Figure 1.3: $|Q_S^{rot}(2_1^+)|$ values of the $2s - 1d$ shell nuclei [11]

The first measurement of $Q_s = -20 \pm 6$ e.fm² by Nakai *et al*, was measured by RE in projectile Coulomb excitation [12]. The rather large bombarding energy of 276 MeV was used, which corresponds to the minimum separation distance of 3.8 fm between the nuclear surfaces of the ³²S and ²⁰⁶Pb nuclei. The γ rays from the excited projectile and target were measured by the NaI counter at the scattering angles (160° and 90°). The scattered projectiles were detected by the particle counter at each angle. This allowed the particle- γ coincidences between the NaI and particle counter. Nakai *et al* experiment was heavily criticized due to the large bombarding energy that was used, which correspond to the relatively small separation distance between nuclear surface. This made the results to be unreliable, since it seemed more likely that the Coulomb excitation had nuclear interferences [11, 13].

The projectile Coulomb excitation experiment of 100 MeV ³²S using ¹¹²Cd target by Häusser *et al*, produced of $Q_s = -17.5.0$ e.fm² [14, 11]. The scattered projectile was detected by the 100 μ m thick annular surface-barrier detector located at 171° and by the 100 μ thick detector located at 70° , while the γ rays from both the excited projectile and target were measure by six 12.7 cm diameter by 15.2 cm long NaI(Tl) detectors. The particle- γ coincidence and angular distribution was used to observe the RE. The bombarding energy used in this experiment corresponded to the hazardous 4.2 fm separation distance between nuclear surface, which renders the results from this experiment unreliable due to the nuclear interferences [11, 13].

Olin *et al* measurement of $Q_s = -6.6 \pm 1.7$ e.fm² was measured using CERE [15, 11]. Olin's experimental setup was very similar to Häusser *et al* experiment. Nevertheless, Olin and co-workers used a rather safer bombarding energy of 100, 112.5 and 125 MeV that corresponds to the minimum separation distances between nuclear surfaces of 6.2 fm on the ²⁰⁴Pb(³²S, ³²S*)²⁰⁴Pb reaction.

However, the results by Olin *et al* were inconsistent with $B(E2)$ values from the Coulomb excitation data by Schwalm *et al* [16].

Ball *et al* bombarded ^{32}S to the ^{208}Pb target with energy 122 MeV, which corresponds to the 6.6 fm separation distance between nuclear surface [17]. RECE was used to measure $Q_s = -11.5 \pm 4.8 \text{ e.f.m}^2$. The spectra was collected from the three laboratory angles of 67° , 130° and 160° . The spectra from the experiment is shown in Fig. 1.4. Such a setup allowed the particle- γ technique for RECE measurements. Although the beam energy used could be considered for RECE, but Spear *et al* mentions that it was not confirmed experimentally for this experiment, therefore the measurements obtained by Ball *et al* cannot be trusted. It is also noteworthy that the roughly 42% uncertainty associated with adopted value of the $Q_S(2^+)$ by Ball *et al* is accepted, however, it remains dubious. This suggests that there is a room for improvement in measurement's accuracy.

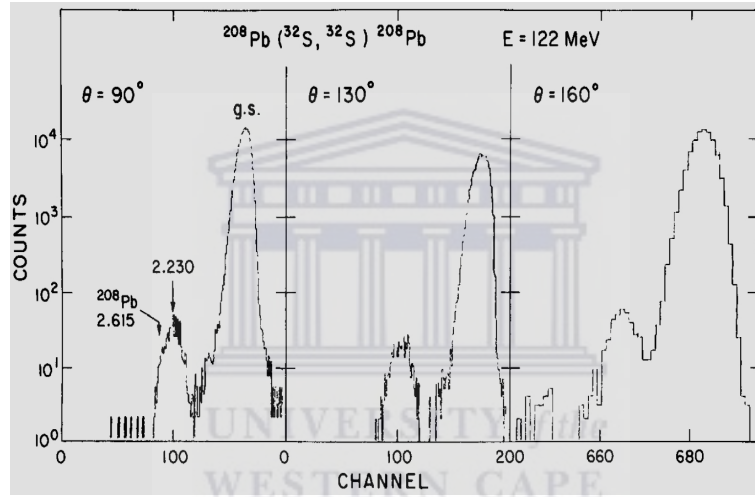


Figure 1.4: Energy spectra for the $^{208}\text{Pb}(^{32}\text{S}, ^{32}\text{S}^*)^{208}\text{Pb}^*$ reaction at different angles [17].

The two most recent experiments of $Q_S(2^+)$ in ^{32}S were done by Vermeer *et al* [13] and Dannhusser *et al* [18]. Vermeer *et al* CERE measurements performed by the bombarding energy of 122-160 MeV yielded results of $Q_S(2^+) = -16.0 \pm 2.2 \text{ e.f.m}^2$. The backscattered ^{32}S ions were measured by the annular silicon detector at the angle of 174° , the ions were also detected at the forward angle of 90° . Dannhusser *et al* $Q_S(2^+)$ in ^{32}S was measured by comparing, in coincidence with ^{32}S ion backscattered from ^{60}Ni , the γ -ray yield of the $2_1^+ \rightarrow 0_1^+$ transition in both nuclei for bombarding energies around 70 MeV. The measured results were $-18.0 \pm 4.0 \text{ e.f.m}^2$ and $-15.0 \pm 4.0 \text{ e.f.m}^2$, depending on the sign of interference term for transitions via the 2_2^+ state in ^{32}S . The experimental results of $Q_S(2^+)$ in ^{32}S are plotted with respect to the years of the experiments in Fig. 1.5 bellow. All of the measurements suggests a prolate shape for the ^{32}S nucleus. However, the scattered measurements on the plot between the earlier and later years suggests poor precision. Whereas, the last three measurements show an improvement on the precision. With the recent improvement on the technology

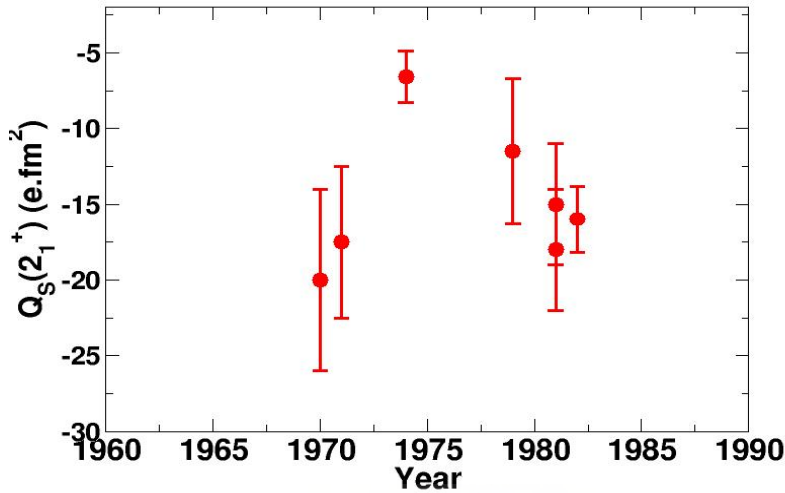


Figure 1.5: Previous measurements of $Q_S(2_1^+)$ values in ^{32}S plotted as a function of published year [11].

for experimental nuclear physics and the measurements improvements from the recent results, more reliable measurements of $Q_S(2_1^+)$ in ^{32}S are desirable.

Recent technology improvements provide state-of-the-art facilities that allow better particle- γ coincidence measurements and Doppler corrections in CERE. Particle- γ and Doppler corrections serve in background subtraction and gamma tuning. Here, these measurements are carried out by the AFRODITE array of clover detectors for γ -ray detection coupled with a double-sided S3 silicon detector for scattered particle detection at iThemba LABS. It is also worth pointing out that a reliable measurement of the $B(E2 : 0_1^+ \rightarrow 2_1^+)$ value is required for the determination of the $Q_S(2_1^+)$ value in ^{32}S . The current adopted $B(E2 : 0_1^+ \rightarrow 2_1^+)$ value from NNDC is $300(13) \text{ e}^2\text{fm}^4$ which was determined from Coulomb excitation experiment and $298(65) \text{ e}^2\text{fm}^4$ was deduced from lifetime measurements [16, 22].

Chapter 2

Theoretical Review

2.1 Coulomb Excitation

Coulomb excitation (CE) is the result of the long-range electromagnetic interaction between two positively charged nuclei. This process occurs when there is an inelastic scattering of nuclei well below the Coulomb barrier. CE has been employed as powerful tool in probing nuclear structure. Due to the well known electromagnetic forces, CE provided measurements with less ambiguity compared to other methods of nuclear reactions. It can populate a single or multiples nuclear states. This research work is interested in populating only the first 2^+ excited state in ^{32}S in order to measure its $Q_S(2_1^+)$.

2.2 Safe Coulomb Excitation

The underlying principle of CE is the prevention of the strong nuclear interaction. Whether or not the nuclear interaction will be prevented primarily depends on E_p . E_p must be chosen in such a way that nuclei interact at a distance apart. Since the CE probability is directly proportional to E_p , then E_p must also be chosen in such a way that it enhances CE probabilities. Therefore, safe CE is achieved when E_p is chosen to prevent nuclear interactions and also enhances CE probability.

2.2.1 Coulomb Barrier

When there is a nuclear reaction, electromagnetic and strong nuclear interactions compete with each other. The strong nuclear forces are dominant at relatively shorts distances between nuclear surfaces. Whereas the electromagnetic forces, Coulomb forces, are dominant at longer distances. The measure of the electromagnetic dominance at longer distance between two nuclei can be done through Coulomb E_{Cb} . The Coulomb force between two nuclei is a repulsive force, preventing the two nuclei to come closer to each other and transitively preventing strong nuclear interactions [23]. Therefore, safe CE requires E_p to be less than E_{Cb} . Assuming that E_{Cb} is maximum when surfaces of the two nuclei touch each other,

$$E_{Cb} = \frac{1}{4\pi\epsilon_0} \frac{Q_p Q_t}{r}, \quad (2.1)$$

where ϵ_0 is the permittivity in free space, r the distance between the center of the two nuclei involved in the reaction, Q_p and Q_t the nuclear charges of the projectile nucleus and target nucleus, respectively. For nucleic reactions, E_{Cb} will be:

$$E_{Cb} = \frac{1}{4\pi\epsilon_0} \frac{Z_p Z_t e^2}{r}, \quad (2.1 a)$$

for Z_p and Z_t being the atomic number of the projectile and target nucleus, respectively. If we use the c.g.s. or Gaussian system,

$$\frac{e^2}{4\pi\epsilon_0} = 1.44 \text{ MeV fm}, \quad (2.1 b)$$

then Eq. 2.1 a becomes,

$$E_{Cb} = 1.44 \frac{Z_p Z_t}{r} \text{ MeV fm}. \quad (2.1 c)$$

It is evident from Eq. 2.1 c that E_{Cb} increases with the increasing of the distance between the two nuclei, as also shown in Fig. 2.1.

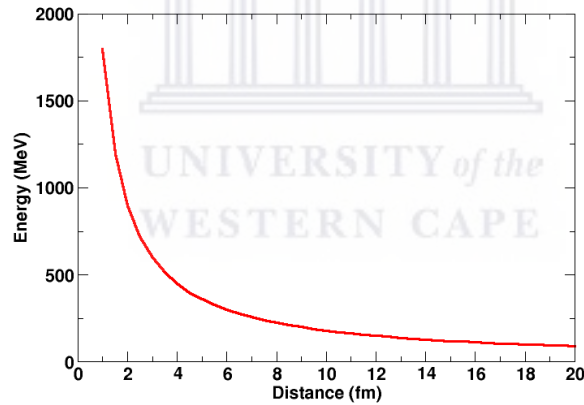


Figure 2.1: Example of Coulomb barrier as a function of the distance between the center of two nuclei.

The strong nuclear interactions dominate the electromagnetic forces, when the distance between the nuclei is relatively small. Assuming that the nuclear interactions are aroused when the nuclear surfaces touch each other, then r will be equal to the sum of radius of both the nuclei. Eq. 2.1 c will be modified to,

$$E_{Cb} = 1.44 \frac{Z_p Z_t}{r_0 (A_p^{\frac{1}{3}} + A_t^{\frac{1}{3}})} \text{ MeV fm}, \quad (2.1 d)$$

with $r_0 = 1.22$ fm. The Coulomb barrier consideration acts as a first step towards “safe” CE.

2.2.2 Distance between nuclear surfaces

The Coulomb barrier plays an important role in safe guarding CE experiment. However, it is only a crude approach to achieve “safe” CE. In addition to the bombarding energy being well below the Coulomb barrier, the distance between nuclear surfaces must be considered. Nuclear interactions are active in extremely short distances of order of 1 fm. This implies that E_p needs to facilitate the safe distance between nuclear surfaces. But this condition should not be ultimately satisfied at the cost of the desired CE cross-sections. CE cross-sections are proportional to E_p [24]. This implies that there is a need of maximizing the CE cross-sections at E_p that separates the nuclear surfaces adequately. Therefore, a distance between nuclear surfaces $S(\vartheta)$ is given by,

$$S(\vartheta) = \frac{0.72Z_pZ_t}{E_p} \left(1 + \frac{A_p}{A_t}\right) [1 + \csc(\vartheta)] - 1.25(A_p^{\frac{1}{3}} + A_t^{\frac{1}{3}})fm, \quad (2.2)$$

where ϑ is the scattering angle in the center-of-mass frame. $S(\vartheta)$ decreases as the E_p and ϑ increases. The minimum distance between nuclear surface S_{min} for “safe” CE was experimentally established and suggested by Cline’s criterion as, $S_{min} = 5 fm$. However, this value has been criticized to be hazardous [25, 26]. Spear *et al* suggested that greater the S_{min} the more safe is the reaction. Thus CE reaction were experimentally suggested to have $S_{min} > 6.5 fm$ [25, 26]. Using Eq. 2.2 and the criteria suggested by Spear, the safe bombarding energy can be determined by using the following equation,

$$E_p = \frac{0.72Z_pZ_t}{S_{min} + 1.25(A_p^{\frac{1}{3}} + A_t^{\frac{1}{3}})} [1 + \csc(\vartheta)]. \quad (2.3)$$

Moreover, it is much recommended that for every CE measurements this needs to be verified [25].

2.3 Semi-classical Approximation

The theory of CE is mathematically complicated to work it out. Due to this reason, some simplified assumptions and approximations are carried out to put less effort to the complicated mathematics [27]. A thoughtful approximation in CE is the semi-classical approximation, which involves the treatment of the projectile motion as if it follows the Rutherford scattering trajectory before and after electromagnetic collision with the target nucleus. This is expected to happen for both elastic and inelastic collisions. As the motion of the target nucleus is treated classically, the excitation of both the projectile and target is treated quantum mechanically, hence the so-called semi-classical approximation.

Since CE involves an inelastic collision, the projectile will lose an excitation energy ΔE_{if} . A necessary condition for the validation of the semi-classical approximation is that ΔE_{if} must be much less than the bombarding energy in the center-of-mass frame E_{cm} . This will ensure that the energy lost by the projectile does not modify the classical trajectory [24].

$$\frac{\Delta E_{if}}{E_{cm}} \ll 1. \quad (2.4)$$

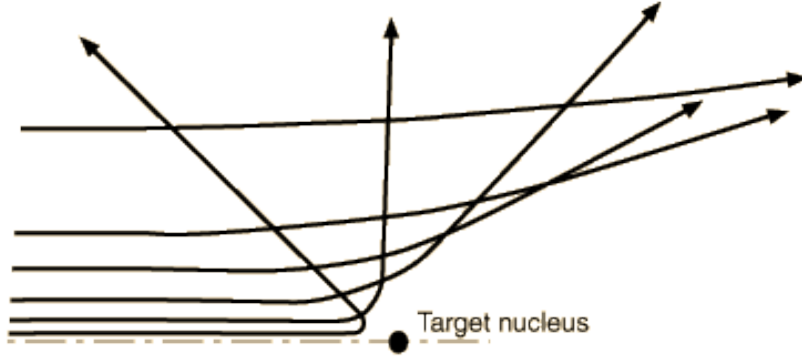


Figure 2.2: Semi-classical approximation where the scattered particle follows a classical hyperbolic trajectory. [28]

2.3.1 Sommerfeld Parameter η

The Rutherford scattering trajectories are governed by the pure Coulomb forces between the projectile and the target nucleus. The Sommerfeld parameter η is a dimensionless number that compares strong nuclear interactions and electromagnetic interactions between two nuclei. This parameter is calculated by taking the ratio of the half distance of closest approach in a head-on collision a and the de Broglie's wavelength λ [29],

$$\eta = \frac{a}{\lambda}. \quad (2.5)$$

Assuming energy conservation on a head-on collision, the kinetic and the potential energies in the center of mass frame are equal,

$$E_{cm} = V_{cm}, \quad (2.5 \text{ b})$$

where,

$$E_{cm} = \frac{1}{2}\mu v_p^2, \quad (2.5 \text{ c})$$

where v_p is the velocity of the projectile in the laboratory frame and

$$\mu = \frac{m_p m_t}{m_p + m_t}, \quad (2.5 \text{ d})$$

is the reduced mass with m_p and m_t the masses of the projectile and target nuclei, respectively. As the Coulomb potential energy is given by,

$$V_{cm} = 1.44 \frac{Z_p Z_t e^2}{b}, \quad (2.5 \text{ e})$$

where b is the impact parameter, then a becomes,

$$a = 1.44 \frac{Z_p Z_t}{\mu v_p^2} \text{ fm}. \quad (2.5 \text{ f})$$

Finally, using Eq. 2.5 d, the Sommerfeld parameter η can be given by,

$$\eta = 1.44 \frac{Z_p Z_t}{\hbar v_p} \text{ MeV fm}, \quad (2.5 \text{ g})$$

where $\lambda = \frac{\hbar}{p_{cm}} = \frac{\hbar}{\mu v_p}$ and $\hbar = \frac{h}{2\pi}$ is the Planck's constant. The semi-classical approximation is fulfilled for $\eta \gg 1$. If $\eta \ll 1$ then $\lambda \gg a$, implying that the process needs to be handled using the Born approximation [24]. The error associated with the semi-classical approximation decreases as η increases.

2.3.2 Adiabaticity Parameter ξ

During CE a nucleus can be excited from an initial state $|i\rangle$ to a final state $|f\rangle$ if the collision time τ is short or approximately equal to the nuclear transition time $\Delta t = \frac{h}{\Delta E_{if}}$, i.e $\tau \lesssim \Delta t$. This allows for a measure of sudden impact vs adiabatic processes, which is characterized by the adiabaticity parameter ξ ,

$$\xi = \frac{\tau}{\Delta t} \lesssim 1 \text{ for a sudden impact collision.} \quad (2.6)$$

The effective time interval for the collision τ can be defined as the time taken by the projectile nucleus to travel a distance $b(\vartheta) = a(1 + \csc(\frac{1}{2}\vartheta))$,

$$\tau(\vartheta) := \frac{2\pi a}{2v_p} (1 + \csc(\frac{1}{2}\vartheta)), \quad (2.6 \text{ a})$$

resulting in ξ dependent on the scattering angle in the center-of-mass frame of reference ϑ ,

$$\xi(\vartheta) = \frac{a \Delta E_{if}}{2\hbar v_p} (1 + \csc(\frac{1}{2}\vartheta)). \quad (2.6 \text{ b})$$

Generally ξ is given for $\vartheta = \pi$,

$$\xi = \xi(\pi) = \frac{a \Delta E_{if}}{\hbar v_p}. \quad (2.6 \text{ c})$$

The CE excitation probability increases when $\xi \lesssim 1$ and decreases exponentially with increasing ξ , as given by the orbital integrals [30]. Finally, using Eq. 2.6 c, the condition for the semi-classical approximation can also be written as,

$$\frac{\Delta E_{if}}{E_{cm}} = \frac{2\xi}{\eta} \ll 1. \quad (2.6 \text{ d})$$

2.4 Coulomb Excitation Cross-sections

The Coulomb-excitation differential cross-section is given by [24],

$$d\sigma_c = P_{i \rightarrow f} d\sigma_R, \quad (2.7)$$

where $P_{i \rightarrow f}$ is the probability of exciting the nucleus from a initial state $|i\rangle$ to the final state $|f\rangle$ via CE, while $d\sigma_R$ is the differential Rutherford scattering cross-section. $P_{i \rightarrow f}$ can be evaluated via time dependent perturbation theory using the time varying electromagnetic potential.

2.4.1 Rutherford scattering cross-sections

The differential Rutherford scattering cross-section is the measure of the probability to elastically scatter the projectile nucleus by the non-moving target nucleus via purely the electromagnetic interaction and is given by,

$$d\sigma_R = \frac{1}{16} \left(\frac{1}{4\pi\epsilon_0} \frac{Z_p Z_t e^2}{E_{cm}} \right)^2 \sin^{-4}(\vartheta/2) d\Omega = \frac{1}{4} a^2 \sin^{-4}(\vartheta/2) d\Omega, \quad (2.8)$$

where Ω is the solid angle. The Rutherford scattering cross-sections decrease as E_{cm} and ϑ increase. This implies that there is an increase of probability to arouse strong nuclear interactions at large bombarding energies and large scattering angles.

2.4.2 First-order Coulomb Excitation

Long-lived nuclear ground state is assumed to be a stationary state [31]. A stationary state produced by a time-independent potential like that of the nuclear ground state, will not make any transition by decay or excitation unless some external potential is introduced into the system. The time-dependent potential $H'(t)$ introduced into this system will induce a transition from an initial nuclear state $|i\rangle = |J_i M_i\rangle$ to the final nuclear state $|f\rangle = |J_f M_f\rangle$ with the transition amplitudes c_{if} . c_{if} can be determined from the first-order time-dependent perturbation theory and give,

$$c_{if} = \frac{1}{i\hbar} \int_{-\infty}^{\infty} \langle f | H(t)' | i \rangle e^{i\omega t} dt, \quad (2.9)$$

where,

$$\omega = \frac{E_f - E_i}{\hbar}, \quad (2.9 \text{ a})$$

where the probability $P_{i \rightarrow f}$ in terms of c_{if} can be written like this,

$$P_{i \rightarrow f} = \frac{1}{2J_i + 1} \sum_{M_i M_f} |b_{if}|^2, \quad (2.9)$$

where M_i and M_f are the magnetic quantum number of the initial and final state, respectively [24]. $H(t)'$ is the external time-dependent potential that causes the nucleus to be excited from the initial state $|i\rangle$ to the final state $|f\rangle$. For CE, the external time-dependent potential is the electromagnetic potential which is generated between the moving projectile and the stationary target which is given in terms of multipole moments,

$$H(t)' = 4\pi Z_p e \sum_{\lambda=1}^{\infty} \sum_{\mu=-\lambda}^{\lambda} \frac{1}{2\lambda + 1} r_p^{-\lambda-1} \times Y_{\lambda\mu}(\theta_p, \phi_p) M^*(E\lambda, \mu), \quad (2.10)$$

for,

$$M(E\lambda, \mu) = \int r^\lambda Y_{\lambda\mu}(\theta, \phi) \rho_n(r) d\tau. \quad (2.10 \text{ a})$$

First-order perturbation theory in CE can be used when light ions are employed as projectile and is possible to extract accurate matrix elements of the multipole operators between two different nuclear states. The differential cross-sections and total cross-sections that result from the first-order perturbation theory are given by [24],

$$d\sigma_{E\lambda} = \left(\frac{Z_p e}{\hbar v} \right)^2 a^{-2\lambda+2} B(E\lambda, J_i \rightarrow J_f) df_{E\lambda}(\theta, \xi), \quad (2.11)$$

$$\sigma_{E\lambda} = \left(\frac{Z_p e}{\hbar v} \right)^2 a^{-2\lambda+2} B(E\lambda, J_i \rightarrow J_f) f_{E\lambda}(\theta, \xi), \quad (2.12)$$

where $df_{E\lambda}(\theta, \xi)$ and $f_{E\lambda}(\theta, \xi)$ are evaluated numerically and are tabulated by Alder and Winther (1956) for $\lambda=1,2,3$ and 4. $B(E\lambda, J_i \rightarrow J_f)$ is the reduced transition probability and is given by,

$$B(E\lambda, J_i \rightarrow J_f) = \frac{|\langle J_f | M(E\lambda) | J_i \rangle|^2}{(2J_i + 1)}, \quad (2.13)$$

Evidently from Eq. 2.11 and 2.12, $B(E\lambda)$ values can be measured via the 1st-order CE cross-sections. First-order CE is applied if $P_{i \rightarrow f}$ is much less than one. To measure the CE cross-sections, the angular distribution of the de-exciting γ rays is carried out for the scattered projectile and is given by [32],

$$W(\theta_\gamma) = \sum_v A_v a_v^{E\lambda}(\eta, \xi) P_v(\cos\theta_\gamma), \quad (2.14)$$

where the constants A_v are said to be the γ - γ directional correlation coefficients tabulated by Bedenharn and Rose (1953) and by Ferentzand Rosenzweig (1955), $a_v^{E\lambda}$ are the particle parameters that depend on the Coulomb excitation process and the Legendre Polynomials $P_v(\cos\theta_\gamma)$, where θ_γ is the between the coming beam and the γ ray.

2.4.3 Second-Order Coulomb Excitation

Second-order CE is the results of determining CE cross-sections via second-order perturbation theory. This method is employed as an appropriate approximation when the first-order perturbation cross-sections are not large enough [32]. For light nuclei used as projectile, first-order is applicable but for heavy nuclei higher-order perturbation approximation like second-order is used to calculate the CE cross-sections. To measure the applicability of the perturbation treatment in CE we introduce the parameter $\chi_{i \rightarrow f}^\lambda$:

$$\chi_{i \rightarrow f}^\lambda = \frac{(16\pi)^{1/2}(\lambda + 1)!}{(2\lambda + 1)!!} \frac{Z_p e}{\hbar(v_i v_f)^{1/2}} \frac{\langle J_f | M(E\lambda) | J_i \rangle}{a_{if}^\lambda (2J_i + 1)^{1/2}}, \quad (2.15)$$

where a_{if}^λ is the symmetrized distance of closest approach in a head-on collision. This parameter measures the strength of the multipole interaction of multipole order λ . If $\chi_{i \rightarrow f}^\lambda < 1$, second-order perturbation treatment can be used[32]. Second-order CE will result in exciting the nuclei to higher nuclear excited state, this is known as the multiple CE. In multiple CE, the nucleus will be excited from the initial state $|i\rangle$ through the intermediate state $|k\rangle$ to the

final state $|f\rangle$.

Beside the multiple CE, the final state $|f\rangle$ will not only depend on the transitional matrix element from the initial state $|i\rangle$ to the final state $|f\rangle$ but will also depends to the diagonal matrix element of the final state $|f\rangle$. This effect is pointing to the static properties of $|f\rangle$ of the nucleus, i.e. the spectroscopic quadrupole moment of the final state $|f\rangle$. This second-order effect is famously known as the reorientation effect (RE) and it is the core discussion of this project.

$\chi_{i \rightarrow f}^\lambda$ is used to describe the theory frame-work of second-order CE and RE. The probability $P_{i \rightarrow f}$ to excite the nucleus from the ground state $|i\rangle$ to the final state $|f\rangle$ via second-order perturbation theory is determined this way

$$P_{i \rightarrow f} = P_{i \rightarrow f}^{(2)} = P_{i \rightarrow f}^{(11)} + P_{i \rightarrow f}^{(12)}, \quad (2.16)$$

where $P_{i \rightarrow f}^{(2)}$ denotes the second-order perturbation, $P_{i \rightarrow f}^{(11)}$ is the first-order perturbation term where is given in terms of $\chi_{i \rightarrow f}^{(2)}$ in this way

$$P_{i \rightarrow f}^{(11)} = \frac{1}{5} [\chi_{i \rightarrow f}^{(2)}]^2 \sum_{\mu=-2}^2 [K_{2,\mu}(\theta, \xi_{if})]^2, \quad (2.17)$$

where

$$K_{2,\mu}(\theta, \xi_{if}) = Y_{2,\mu}(\frac{\pi}{2}, 0) I_{2,\mu}(\theta, \xi_{if}), \quad (2.17 \text{ a})$$

$Y_{2,\mu}(\frac{\pi}{2}, 0)$ are spherical harmonics and $I_{2,\mu}(\theta, \xi_{if})$ are Alder's classical orbital integrals [33, 34]. Taking into account Eq. 2.13 and 2.15, assuming that a projectile nucleus will be excited via CE from the ground state with $J_i^\pi = 0^+$ to the excited state $J_f^\pi = 2_1^+$, then Eq. 2.17 will be modified to,

$$P_{i \rightarrow f}^{(11)} = 1.61 \left(\frac{Z_p e}{\hbar \sqrt{v_i v_f} a_{if}^2} \right)^2 B(E2) \sum_{\mu=-2}^2 [K_{2,\mu}(\theta, \xi_{if})]^2, \quad (2.17 \text{ b})$$

$P_{i \rightarrow f}^{(12)}$ is given by,

$$P_{i \rightarrow f}^{(12)} = \frac{27\pi^{\frac{3}{2}}}{\sqrt{5}} \chi_{f \rightarrow f}^{(2)} [\chi_{i \rightarrow f}^{(2)}]^2 \sum_{\mu=-2}^2 [K_{2,\mu}(\theta, \xi_{if})]^2 B_{2\mu}^{(22)}(\xi_{if}, 0, \vartheta), \quad (2.18)$$

where,

$$\chi_{f \rightarrow f}^{(2)} = \frac{1}{3} \sqrt{\frac{7}{10}} \frac{Z_p e^2 Q_S(2_1^+)}{\hbar v_p a_{if}}, \quad (2.18 \text{ a})$$

Defining,

$$k_1(\vartheta, \xi_{if}) = \left(\frac{8\sqrt{\pi} Z_p e}{\hbar \sqrt{v_i v_f} a_{if}^2} \right)^2 K_1(\vartheta, \xi_{if}), \quad (2.18 \text{ c})$$

$$k_2(\xi_{if}, 0, \vartheta) = \sqrt{\frac{7}{50}} \frac{9\pi^{\frac{3}{4}} Z_p e^2}{\hbar v_p a_{if}} B_{2\mu}^{(22)}(\xi_{if}, 0, \vartheta), \quad (2.18 \text{ d})$$

Therefore the probability $P_{i \rightarrow f}^{(2)}$ becomes,

$$P_{i \rightarrow f}^{(2)} = B(E2)k_1(\vartheta, \xi_{if})(1 + Q_S(2^+)k_2(\xi_{if}, 0, \vartheta)), \quad (2.19)$$

This equation leads to the RE cross-sections,

$$\left(\frac{d\sigma_c}{d\Omega}\right)_{i \rightarrow f} = \left(\frac{d\sigma_R}{d\Omega}\right)P_{i \rightarrow f}^{(2)}, \quad (2.20)$$

$$\sigma_c = \sigma_R[B(E2)k_1(\vartheta, \xi_{if})(1 + Q_S(2^+)k_2(\xi_{if}, 0, \vartheta))]. \quad (2.21)$$

The Eq. 2.21 shows the Coulomb excitation reorientation effect (CERE) cross-sections which primarily depend on the Rutherford scattering cross-sections, $B(E2)$ value, spectroscopic quadrupole moment, adiabaticity parameter and the center-of-mass scattering angles. The significant observable that affects the CERE cross-sections is the $Q_S(2_1^+)$. CERE is the 2^{nd} -order effect in Coulomb excitation which causes the hyperfine split of magnetic substates, where the population of the different substates is changed by the presence of the $Q_S(2_1^+)$. According to Eq. 2.21, if the $Q_S(2_1^+) < 0$ (prolate shape) the CERE cross-sections are decreased and if the $Q_S(2_1^+) > 0$ (oblate shape) CERE cross-sections are increased.

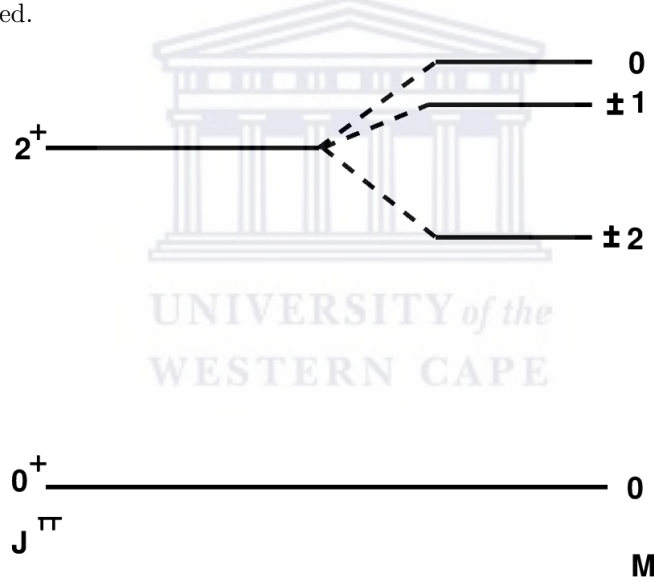


Figure 2.3: The orientation of the magnetic substates is affected by a prolate shape.

2.5 Nuclear Models

A nucleus is a many-body problem system. Many-body problem in quantum mechanics is a much complicated system to solve. Due to this reason nuclear structure utilizes nuclear models as an attempt to describe the behaviour of a nucleus. Models are characterized by the nuclear observables like energy, angular momentum, nuclear moment, etc. Two popular models in nuclear physics are discussed in relation to the interest of this research.

2.5.1 Shell Model

Shell model is a first step in looking at the quantum nature of the nucleus. This is described in terms of energy, angular and the use of Pauli's exclusion principle. It was established through the attempt of explaining special nucleon numbers called magic numbers [35]. Nuclei with nucleon number equal to that of any of the magic numbers is super stable than their neighboring nuclei. This is shown by the experimental values of binding energy per nucleon B/A of nuclei with Z or N equal to some several magic numbers which deviates from the semi-empirical mass formula curve. Fig. 2.4 below shows this effect.

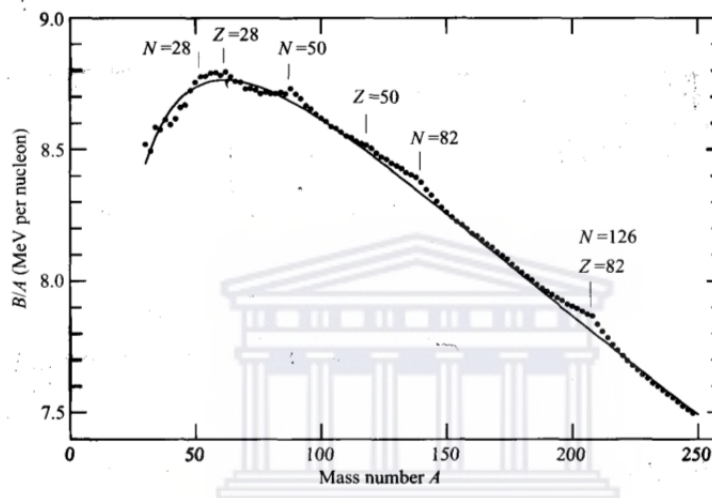


Figure 2.4: Binding energy per nucleon B/A as a function of mass number A [36].

Moreover, the single-nucleon separation energy curve in Fig. 2.5 shows some sharp spikes on nuclei with magic numbers.

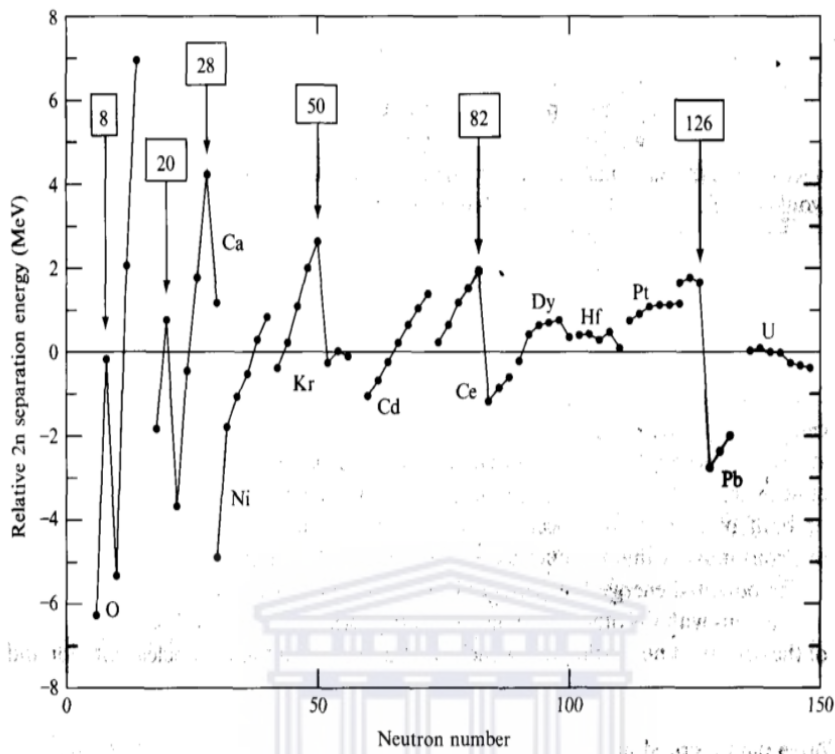


Figure 2.5: $S(2n)$ separation energy as a function of neutron number N [37].

The underlying principle of the shell model was to describe the nuclear states in terms of nucleon degrees of freedom [38]. The calculations started with the assumption of the single-particle states. Like any quantum mechanical system, a need of selecting a potential which governs this system was crucial. For simplicity, a quantum harmonic oscillator was selected for the shell model which produced energy levels showed in Fig. 2.6.

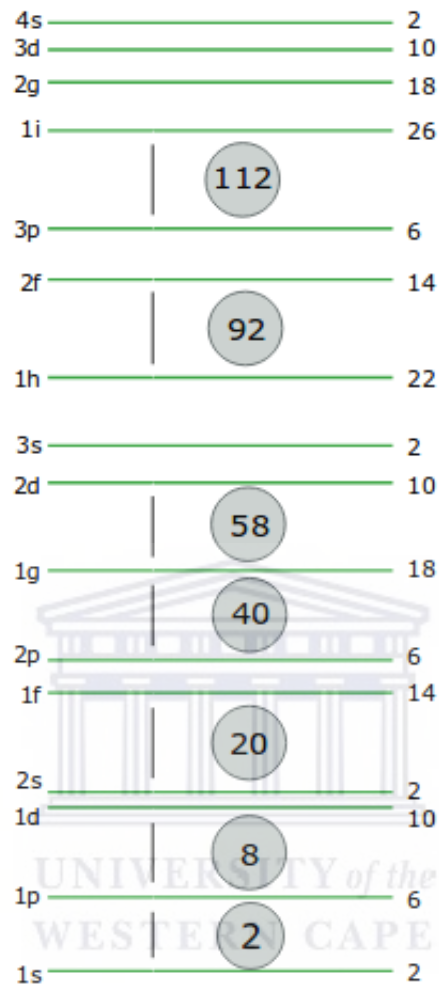


Figure 2.6: Energy levels produced by the quantum harmonic oscillator [39].

The quantum harmonic oscillator potential could not produce all the magic numbers and this led into looking for a more realistic potential. Spin-orbit interaction is incorporated in the system to accommodate the entire magic numbers. This phenomenon had an ability to split the existing energy levels from quantum harmonic oscillator and thus accounting the missing magic numbers [40]. Fig. 2.7 shows the effect of the spin-orbit interaction on the quantum harmonic oscillator energy levels.

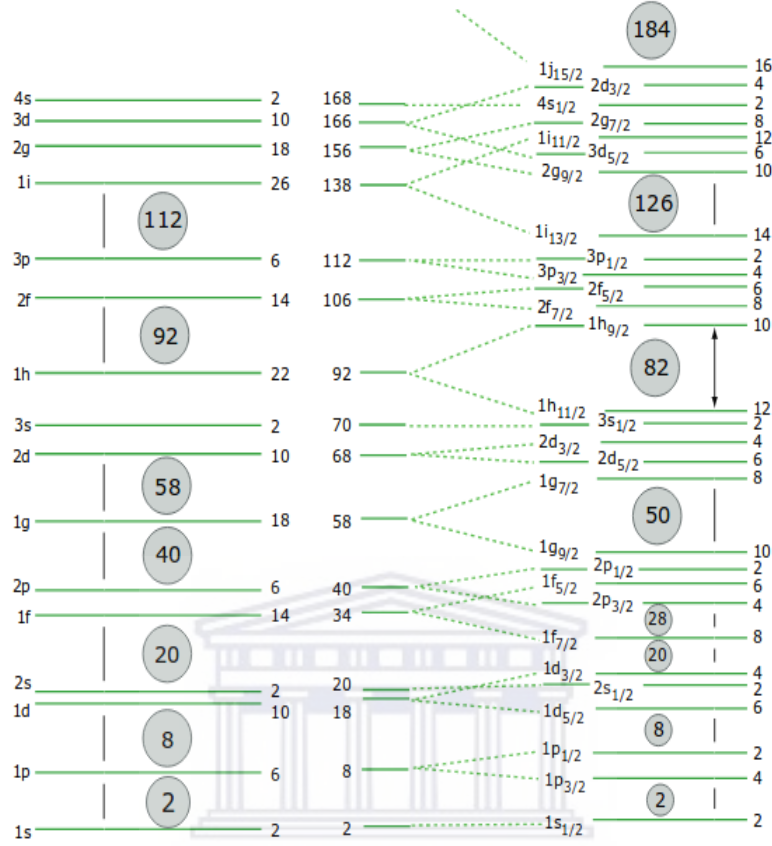


Figure 2.7: Effects of spin-orbit interaction on quantum harmonic oscillator potential energy levels [39].

Shell model is generally known of the phenomenon called the extreme independent particle model which basically assumes that all nucleons but one are paired and the nuclear properties are governed by the motion of the single unpaired nucleon [41]. Implying that nuclear moments need to be defined in terms of single particle shell model. For shell model calculations, the electric quadrupole moment operator Q_0 is carried for the odd proton in a state in which the total angular momentum of the proton has its maximum projection along the z-axis, i.e. $m = J$. The reason the Q_0 is applied on the proton only, it is assumed that it is zero for the neutron since it is chargeless. Therefore, for a single proton, electric quadrupole moment will be [42],

$$Q_{sp} = -\frac{2J-1}{2J+1} \langle J|r^2|J \rangle, \quad (2.22)$$

where the radial average is given by,

$$\langle J|r^2|J \rangle = \int r^4 R_{nJ}^2 dr. \quad (2.22 \text{ a})$$

Shell model state	Calculate Q_S (b)	Measured Q_S (b)
1p _{3/2}	-0.013	-0.0366(⁷ Li)
1d _{5/2}	-0.036	-0.12(¹⁹ F)
1d _{3/2}	-0.037	-0.08249(³⁵ Cl)
1f _{7/2}	-0.07	-0.26(⁴³ Sc)
2p ₂	-0.055	-0.209(⁶³ Cu)
1f _{5/2}	-0.086	
1g ₂	-0.13	-0.32(⁹³ Nb)
1g _{7/2}	-0.14	-0.49(¹²³ Sb)
2d _{5/2}	-0.12	-0.36(¹²¹ Sb)

Table 2.1: A table of shell model calculations of Q_s and experimental values [41].

In table 2.1, the shell model calculations of Q are calculated using Eq. 2.22. It was successful in predicting quadrupole moments of some nuclei in their ground states but it failed to predict quadrupole moments observed for heavy nuclei [43].

2.6 Collective Model

Nuclear collectivity is more evident when one considers the excitation of even-even nuclei. This is because even-even nuclei with ground state 0^+ have a low first excited 2^+ state which cannot be explained by the shell model. The low first excited state 2^+ can be explained by assuming that a nucleus is excited as a collective body. Nuclear collectivity is much associated with the shape of the nucleus. The shape of the nucleus is described in terms of expansion of the nuclear surface into spherical harmonics,

$$R(\theta, \phi, t) = R_0 \left(1 + \sum_{\lambda\mu} \alpha(t)^* Y_{\lambda\mu}(\theta, \phi) \right). \quad (2.23)$$

Therefore, the excitation of the collective nucleus is either by vibrational, rotational or exhibits both features.

2.6.1 Rotational States

Collective rotational motion of a nucleus is known to exist in nuclei with a non-spherical shape. Spherical nuclei are known not to be able to rotate in quantum mechanics, since there is no change that can be detected when it rotates. Moreover, a nucleus is not allowed to rotate about its axis of symmetry. The nucleus thus rotates about the axis perpendicular to the axis of symmetry. One of the observable that is used to measure directly the deformation of the nucleus from its sphericity is the quadrupole moment.

A rotating nucleus will produce an angular momentum called rotational angular momentum \mathbf{R} . In addition to the rotational angular momentum is the intrinsic angular momentum \mathbf{J} , which is sum of the individual angular momentum of the nucleons. Therefore, the total angular momentum of the system \mathbf{I} will be the sum of \mathbf{R} and \mathbf{J} . Even-even nuclei with spin 0^+ in their ground state they have

a rotational angular momentum equal to the intrinsic angular momentum \mathbf{J}^+ . The projection of \mathbf{I} on the axis of symmetry is \mathbf{K} . The rotation energy is derived from the classical relation,

$$E(j) = \frac{1}{2}Iw^2 = \frac{(Iw)^2}{2I} = \frac{j(j+1)\hbar^2}{2I} - \frac{K^2\hbar^2}{2I}, \quad (2.24)$$

where j is the total angular momentum quantum number for J , I is the moment of inertia and w is the angular frequency. The ground state of an even-even rotational nucleus has $K=0$.

2.6.2 Vibrational States

Describing the shape of the nucleus by Eq. 2.23, the vibrational states will be the compression and relaxation of the nucleus while it maintains the same volume. There are three kinds of small vibrational modes, namely, dipole, quadrupole, and octupole mode. All of the three vibrational modes are described by the difference in λ value.

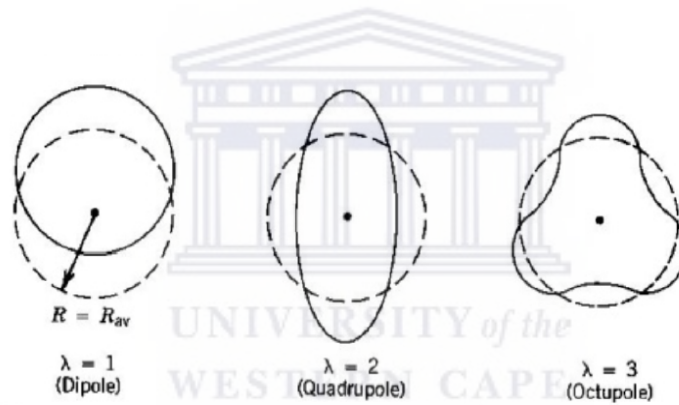


Figure 2.8: Lowest modes of vibration.

Dipole mode $\lambda=1$

Dipole vibrational mode is the displacement of the center of the nucleus without any change in the surface of the nucleus. During the dipole vibrational mode the shape of the nucleus remains unchanged.

Quadrupole mode $\lambda=2$

Quadrupole mode is associated with the quadrupole deformation and the quadrupole deformation is associated with the well known electric nuclear quadrupole moment. This mode is considered to be the important mode of vibration. For it is the most evident in nuclear vibrational excitation. Quadrupole vibrational mode of excitation happens by accepting quantized amounts of energies called phonons. A phonon that is associated with the quadrupole mode nuclear vibrational excitation is called quadrupole phonon. A phonon is basically defined as

$$E = \hbar w, \quad (2.25)$$

where w is the angular frequency. Energy of every vibrating nucleus will be a multiple of a phonon, which is described by Eq. 2.24. One phonon state for a quadrupole mode vibrations will be 2^+ state. Two phonon state will be either 0^+ , 2^+ or 4^+ .

Octupole mode $\lambda=3$

The octupole mode vibrating nucleus has first excited spin equal to 3^+ and the next excited states are either $0^+, 2^+, 4^+$ or 6^+ . Octupole mode vibrations are not extensively studied leading to the least known mode of vibration compared to the quadrupole mode.



Chapter 3

Experimental Details

The $^{194}\text{Pt}(^{32}\text{S}, ^{32}\text{S}^*)^{194}\text{Pt}^*$ CE experiment was performed at the iThemba LABS facility. The ^{32}S ion beam with energy 120.3 MeV was bombarded on ^{194}Pt with $1\text{mg}/\text{cm}^2$ thickness. This experiment was performed using S3 double-sided silicon detector (S3-detector) for back-scattered particles together with the AFRODITE High-Purity-Germanium (HPGe) clover array to detect gamma rays. The choice of the heavy ^{194}Pt target was because of the known reduced transitional probabilities of the transition from the ground state 0^+ to the first 2^+ excited state in ^{194}Pt .

3.1 Experimental Design

In this section necessary limitations and prerequisites for the CE experiment to be successful, are discussed. These limitations and prerequisites are defined according to the detectors and experimental set-up that will be used specifically for this experiment.

3.1.1 “Safe” Beam Energy

The basic assumption for CE is that the interaction between the target and the projectile is purely electromagnetic in nature [44]. This is accomplished by few assumptions that need to be considered concerning the “safe” beam energy E_p . The assumptions are discussed in Chapter 2. The first assumption is that,

$$E_p < E_{CB} , \quad (3.1)$$

where

$$E_{CB} = 1.44 \frac{Z_p Z_t}{r_0 (A_p^{\frac{1}{3}} + A_t^{\frac{1}{3}})} \text{MeV.fm} = 164.0 \text{ MeV} , \quad (3.1 \text{ a})$$

and this satisfy the Coulomb barrier preliminary condition, since $E_p = 120.3 \text{ MeV} < 163.97 \text{ MeV}$.

Safety of the CE experiment also lies in the distance between nuclear surfaces $S(\vartheta)$,

$$S(\vartheta) \geq 6.6 \text{ fm} , \quad (3.2)$$

and this is verified in Fig. 3.1.

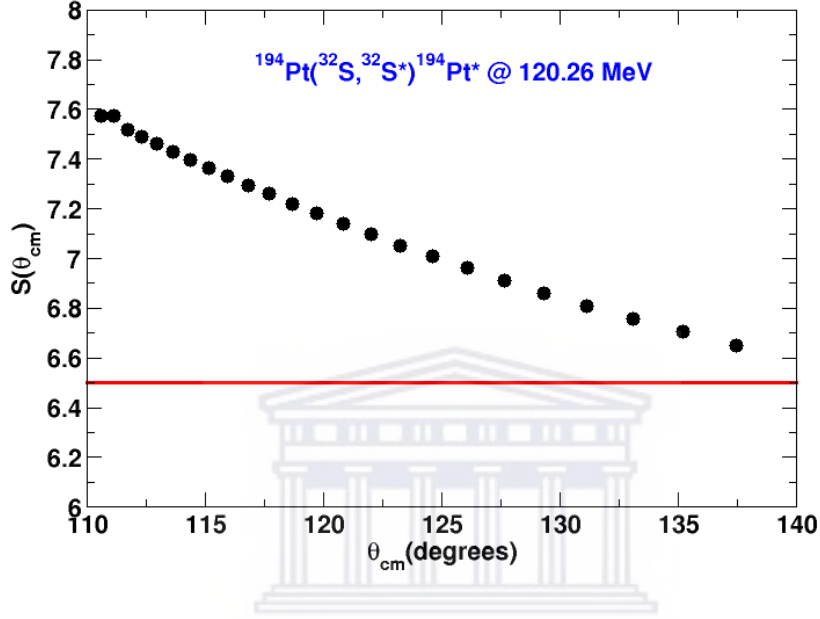


Figure 3.1: Showing the distance between nuclear surfaces as a function of laboratory scattering angles for 120.3 MeV beam energy.

Using the confirmation from Fig. 3.1, E_p is determined this way,

$$E_p = \frac{0.72Z_pZ_t}{S + 1.25(A_p^{\frac{1}{3}} + A_t^{\frac{1}{3}})} [1 + \csc(\vartheta)] , \quad (3.3)$$

giving

$$E_p = 120.3 \text{ MeV} . \quad (3.3 \text{ a})$$

Clearly the E_p obtained is reliable for CE experiment since it is less than our Coulomb barrier from equation 3.1 a. and it separates the nuclear surfaces reasonably.

3.1.2 Semi-Classical Approximation

The semi-classical approximation commands the projectile nucleus to go a classical hyperbolic path during the coulomb collision. This approximation is predicted using the Sommerfeld η and the adiabaticity parameter. The Sommerfeld parameter according to Section 2.1.2 is given by

$$\eta = \left(1 + \frac{A_p}{A_t}\right) \frac{Z_pZ_t}{\hbar v_p} 1.44 \text{ MeV}\cdot\text{fm} = 118, \quad (3.4)$$

$\eta \gg 1$ satisfies the semi-classical approximation requirement for this CE experiment. Adiabaticity parameter assumes that E_p must be much greater than the excitation energy, i.e.

$$\frac{\Delta E_{if}}{E_{cm}} < 1, \quad (3.5)$$

which is

$$\frac{\Delta E_{if}}{E_{cm}} = 0.0215, \quad (3.5 \text{ a})$$

The adiabaticity parameter curve calculated by Eq. 2.6 b is shown in Fig. 3.2

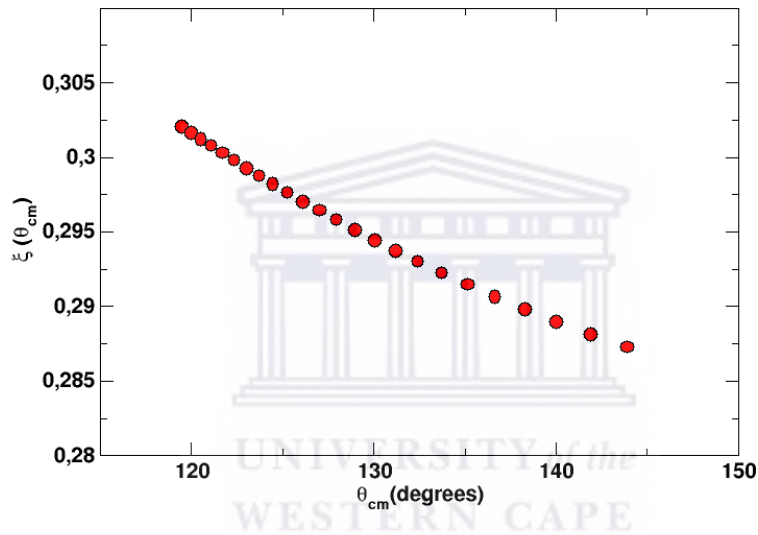


Figure 3.2: The adiabaticity parameter as function of center-of-mass angles.

3.2 Particle and Gamma ray Detection

Information from the nuclear reaction is mostly known through the radiation emitted by the product nuclei of the reaction. Radiation emitted interacts with the material of the detector to be detected. The interaction causes the radiation to lose its energy as it travels through the material of the detector [46]. There are two kinds of radiation of interest in this research work, namely, charged particles and γ -rays. Charge particle and γ -ray detectors are built according to the respective modes of interactions, thus the modes of interactions will give the detectors their specific characteristics. The main interactions of charged particles with the material of the detector are ionization and excitation, while the gamma-rays interact by photoelectric effect, Compton Scattering and pair production.

3.2.1 Heavy Charged Particle Detection

Heavy charged particles interact with matter through Coulomb forces between their positive charge and the negative charge of the orbital electrons within the atom of the material of the detector [46]. During these Coulomb interactions, the electrons of the material of the detector either gain energy to be excited to a higher-lying shell within the atom or gain a reasonable energy to be totally removed from the atom, thus ionizing the atom [47]. The energy which is gained by the electron is transferred from the incident heavy charged particles. Ionization creates two different products, depending to the detector material. In gas-filled detectors electrons-ion pairs are created and collected by the two electrodes and the signal is established, while in semiconductor/solid state detectors electron-hole pairs are created and the electrons are collected in the positive electrode and the holes are collected in the negative electrode. By this process the signal is established.

3.3 Gamma-ray Detection

Radioactive nuclei emit three types of ionizing radiation, α particles, β particles and γ -rays. Gamma-rays are massless, chargeless and very energetic. Just like any other radiation, γ -rays also have an ionizing ability and are essential in revealing the nuclear structure. γ -rays interacts with the material of the detector through the ionizing ability it has. Ionization happens indirectly through these mainly three interactions, namely, photoelectric effect, Compton scattering and pair production.

3.4 AFRODITE

African Omnipurpose Detector for Innovative Techniques and Experiment (AFRODITE) is an array of 16 γ -ray detectors, 8 High Purity Germanium (HYGe) detectors and Low Energy Photon (LED) detectors. LED were not used for this experiment, so they are not discussed. AFRODITE is medium size array and has a rhombicuboctahedron frame to compensate the 16 γ -ray detector. At the center of the AFRODITE detector lies the rhombocuboctahedron target chamber to fit with 16 photon detector. The target chamber has a capacity to accommodate S3 Silicon detector used for particle detection. Through from the top of the target there is a electronic target ladder for target selection.

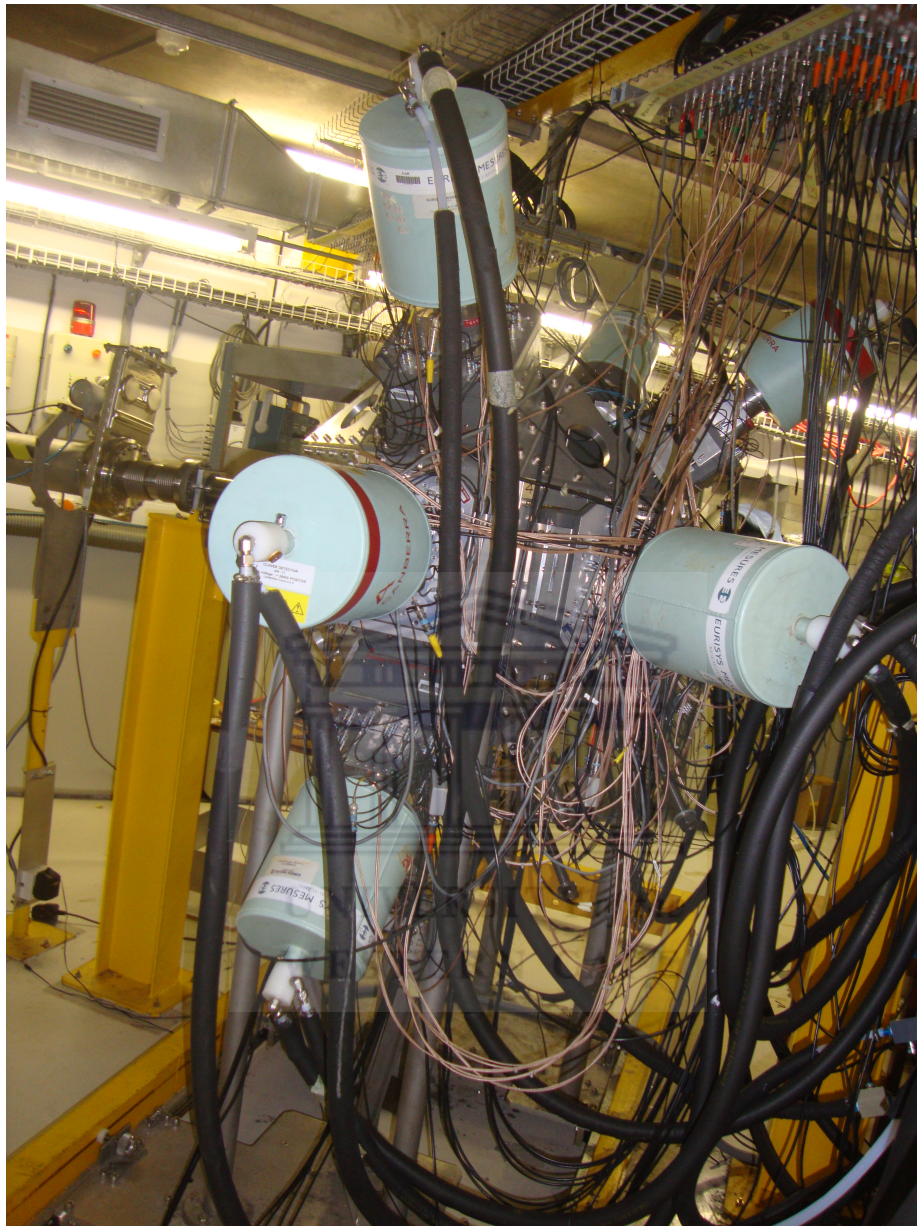


Figure 3.3: ARODITE Array.

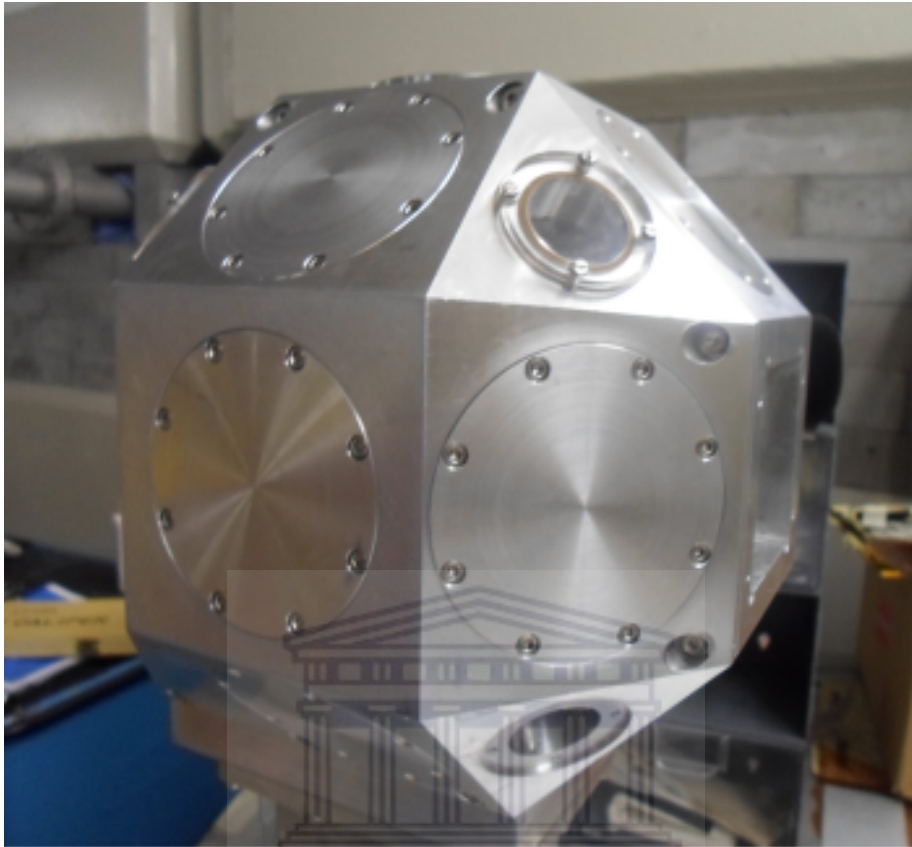


Figure 3.4: Target Chamber.

3.4.1 Clover Detector

Eight large volume HPGe clover detectors are 19.6 cm away from the target frame and are positioned with known angles with respect to the beam line. This is crucial for Doppler correction calculations. They have a capability of detecting high energy photons with reasonably high efficiency. Each Clover detector has four separate 50×70 mm HPGe crystals. Each of the HPGe crystal has a front diagonal diameter of 50 mm, 41 mm front width, 36 mm tapering length, length of 70 mm and there is a separation distance of 0.2 mm between two crystals. The small distance between two crystals is meant to improve the add-back factor [53]. Crystals are electronically connected independent to allow independent signal output [54].

For good operation, Clover detector are to be at the temperature of -180 °C. Clover detector temperatures are monitored and controlled by an automated electronic system. To ensure this, each Clover detector has a 2.5 liter liquid nitrogen dewar which is connected to the crystals via copper rod for continuous cooling. PTFE tubes and solenoid-operated valves are used to fill the via detectors with liquid nitrogen from the 180 liter liquid nitrogen tank supply.

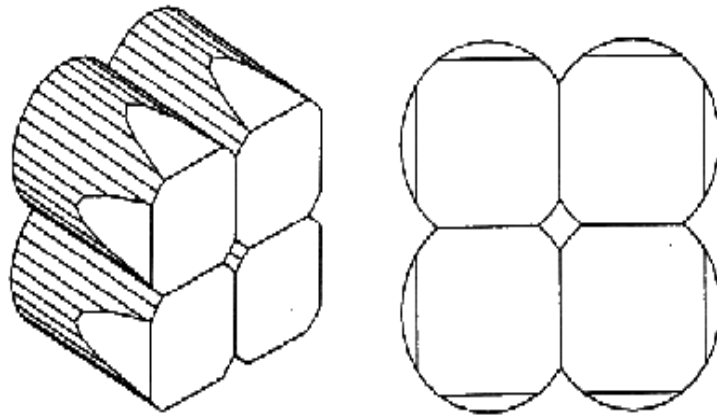


Figure 3.5: Schematic representation of the HYGe clover crystals [55].

Each clover detector is surrounded by the Bismuth Germanate (BGO) detectors. BGO detectors are Compton Suppressor shields for germanium detectors that are used to reduce background. Because gamma rays are either fully absorbed or scattered by the detector and the scattered gamma rays contribute to the background, BGO detectors detect scattered gamma rays. Fig. 3.6 shows a typical clover detector.



Figure 3.6: A typical Clover detector

3.4.2 S3 Silicon Detector

A target chamber which is located at the center of the AFRODITE array, can be coupled with the S3 silicon detector. Figure 11. shows the S3 detector inside the target chamber. S3 Silicon detector is used to detect scattered charged particles. This detector was placed before the target to detect back-scattered charged particles since the Reorientation Effect is most sensitive at backward angles. It has a shape similar to that of a compact disk with the inner diameter of 22 mm and outer diameter of 70 mm. The inner hole with 22 mm diameter allows the incident beam to pass through without damaging the detector. The detector has double sides of 24 micro-strip rings on the other side and 32 segmented sectors on the other side.

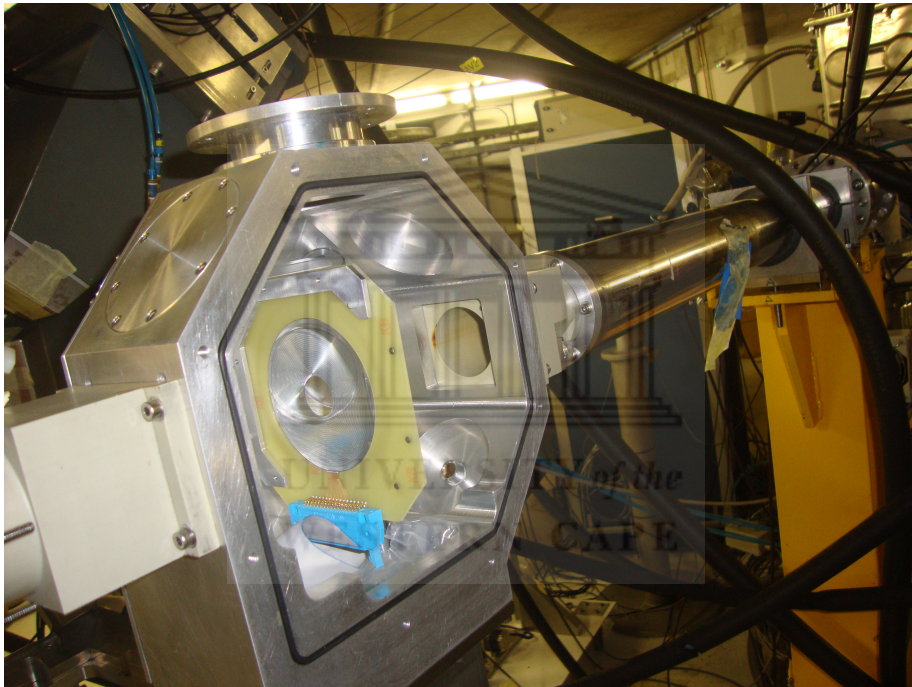


Figure 3.7: S3 Silicon detector inside the target chamber

The S3 silicon detector detects the energy deposited by the charged particle and the position of the hit, thanks to coupling of the rings and sectors. For CE experiment, rings are essential for γ -ray angular distribution with respect to the scattering angle of the incident beam and Doppler corrections for the γ -rays and the sectors are also essential for Doppler corrections for γ -rays. Each ring has a width of 0.886 mm while each of the sectors possess a width suspended by the angle of 11.25° . Rings are connected on the junction side while the sectors are connected on the ohmic side. The detector produces two signal formation, one from the rings and one from the sectors. Fig. 3.8 shows the schematic S3 detector with specified dimensions.

AFRODITE array coupled with the S3 silicon detector provides a state-of-art fa-

cility for Coulomb excitation experiment. This advantage will produce accurate and reliable RE measurements for $^{196}\text{Pt}(^{32}\text{S}, ^{32}\text{S}^*)^{196}\text{Pt}^*$ CE experiment.

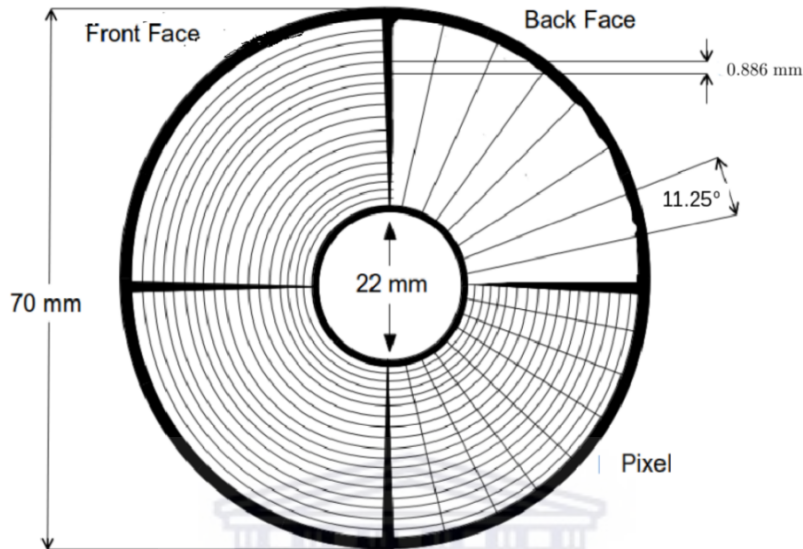


Figure 3.8: Schematic drawing of S3 silicon detector[56]

3.5 Electronics and Data Acquisition System

The electronic signal from the detector material needs to be transported and collected via a complete electronic circuit. Clover detectors have a separate electronic connection from the S3 silicon detector electronic connection. This allows an independent signal collecting for both the detectors.

Signal collection from the S3 silicon detector is done by transportation of the signal created in the rings and sectors through the 4 Metysec mesh-shielded cables labeled R1, R2, S1 and S2. R1 and R2 cables are responsible for the transportation of the signal from the 24 ring and S1 and S2 cables are responsible for the transportation of the signal from the 32 sectors. Each of the R1, R2, S1 and S2 accept 16 signals. From the S3 silicon detector, the R1, R2, S1 and S2 cables connect to the 2 MPR-32 multichannel preamplifier. MHV-4 bias was used to power up the 2 MPR-32 preamplifiers.

MPR-32 and MHV-4 are readout electronics manufactured by Metysec for multi-channel modules. These are designed for double sided multistrip silicon detector, e.g. S3 silicon detector. MPR-32 preamplifier are used to amplify the output signal created when the charged particle deposits its energy to the S3 silicon detector. Through this, noise will be discarded even at low charge deposition[57]. MHV-4 is a bias supply voltage for a detector with 4 channel. It supplies a bias voltage up to 400 V and this voltage can be adjusted manually. This device is

designed to show the leakage current increment over time to prevent the damage of the S3 silicon silicon detector[58].

The signals from the four preamplifiers are then transported to a XIA based digital system consisting of two PXI crates. The amplified electronic signals are digitised in the multiple 16-channel DGF Pixie-16 modules which are contained on the two PXI crates. Two DGF Pixie-16 modules were receiving electronic signals from the γ ray clover detectors and four of the modules were receiving electronics signals from the particle S3 silicon detector. The processed and digitized signals are sent to the computer running MIDAS software data acquisition system. Fig. 3.9 showing the electronic setup at iThemba LABS.

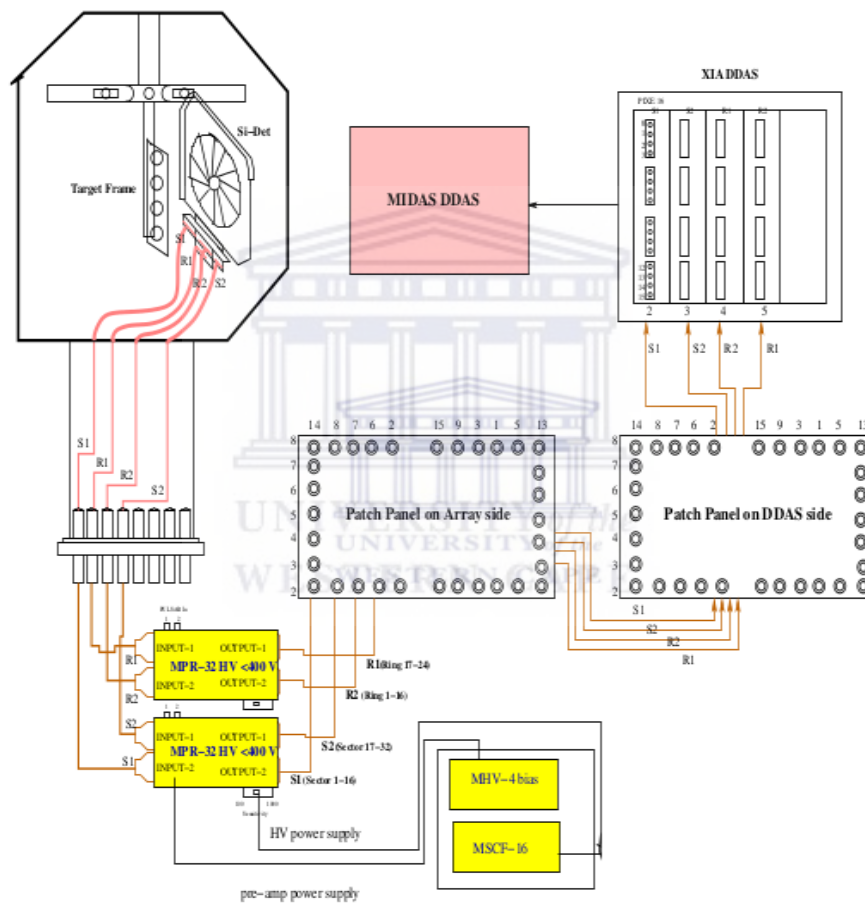


Figure 3.9: Sketch of the electronics setup for Coulomb-excitation experiments at iThemba LABS [56].

Chapter 4

Analysis and Results

4.1 Calibration

4.1.1 Efficiency Calibration

In radiation detection, like γ -ray detection, efficiency is one of the most important characteristic of the detector. This is due to the fact that it reveals directly the performance of the detector itself. Since some of the γ -rays does interact with material of the detector without producing a signal, implying that there is no detector with 100% efficiency [59]. Detector efficiency is the probability to detect an emitted γ -ray. In a nutshell, it is the percentage of the radiation that a detector detects from the total emitted γ -rays by the source.

Detector efficiency depends on the absorption cross-section in the material of the detector, distance and position from the source to the detector, volume and shape of the detector material. Detector efficiency definition can be mainly categorized into two descriptions, namely, absolute and intrinsic efficiency [59]. The absolute efficiency is defined as,

$$\epsilon_{abs} = \frac{\text{number of pulses recorded}}{\text{number of radiation quanta emitted by the source}}. \quad (4.1)$$

The absolute efficiency depends on the detector properties and also on the setup of the detector system, such as the distance between the detector (solid angle Ω) and the source. The intrinsic efficiency is defined as,

$$\epsilon_{int} = \frac{\text{number of pulses recorded}}{\text{number of radiation quanta incident on detector}}. \quad (4.2)$$

The intrinsic efficiency is independent of the detector system setup. The solid angle does not affect the intrinsic efficiency.

With respect to this experiment, ^{152}Eu and ^{56}Co sources were placed on the target ladder inside the scattering chamber after the experiment to collect the AFRODITE clover array efficiency calibration data. The data was collected and processed by the MIDAS MTsort software.

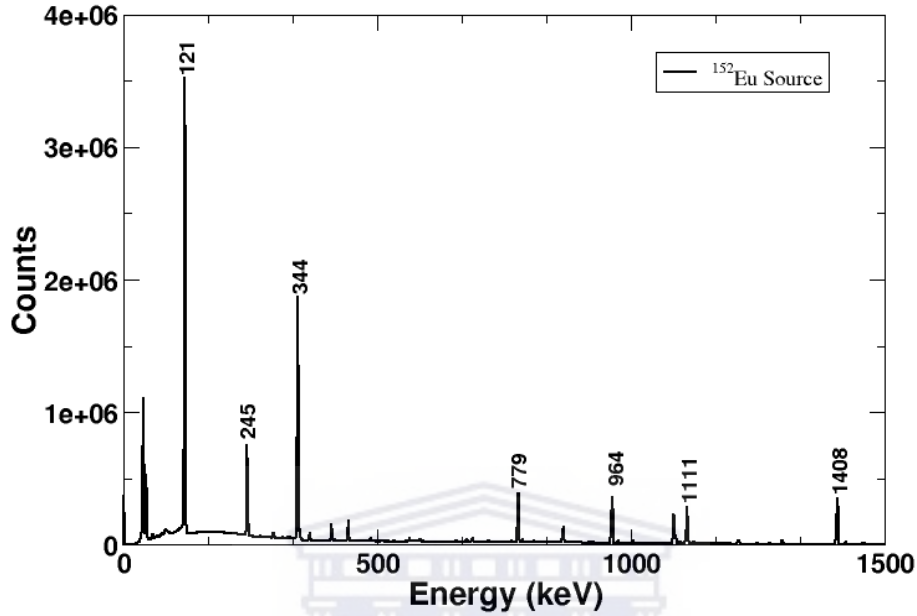


Figure 4.1: ^{152}Eu calibration spectrum.

Figure 4.1 and Figure 4.2 show the efficiency calibration spectra of ^{152}Eu and ^{56}Co sources, respectively.

The MIDAS Mtsort data was then converted by eg2rad command to the .spe file so that it can be readable to the RADWARE software. RADWARE gf3 was used to read the .spe spectrum and then .sto files were created. The .sto files which have the peaks energies and their areas of both the ^{152}Eu and ^{56}Co sources were used to create the .sin files using the Source command in RADWARE. The .sin file are the files required in effit to do the efficiency calibration. To do efficiency calibration, the measured efficiency is fitted to the relative efficiency equation,

$$\ln(\epsilon) = ((A + Bx + Cx^2)^{-G} + (D + Ey + Fy^2)^{-G})^{-\frac{1}{G}}, \quad (4.3)$$

where A , B and C describe efficiency at low energies and D , E and F describe efficiency at higher energies, G is the interaction parameter between lower and higher energy region, whereas x and y are defined as follow,

$$x = \ln\left(\frac{E_\gamma}{E_0}\right), \quad (4.3 \text{ a})$$

$$y = \ln\left(\frac{E_\gamma}{E_0}\right), \quad (4.3 \text{ b})$$

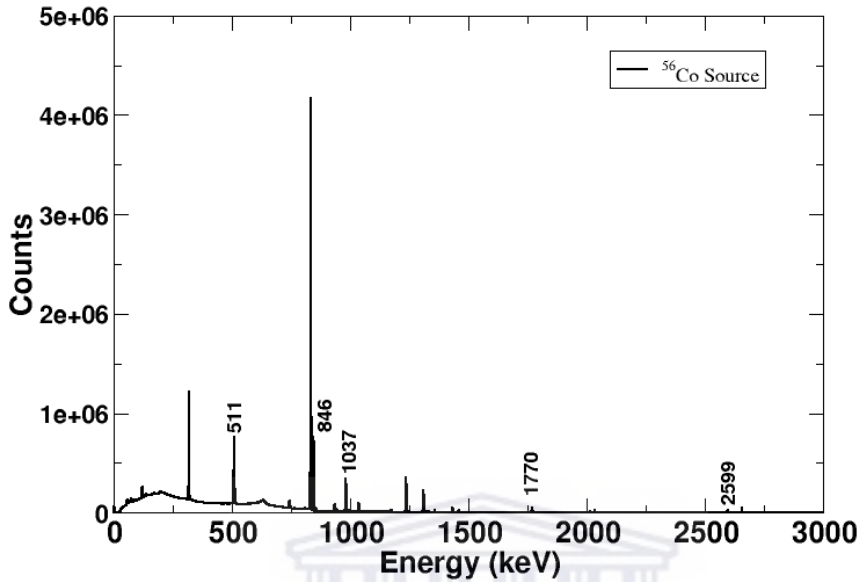


Figure 4.2: ^{56}Co calibration spectrum.

where $E_0=100$ keV for lower energy and $E_0=1000$ keV for higher energies. The resulting relative efficiency curve is shown in Figure 4.3.

4.1.2 HPGe Clover Detector Energy Calibration

^{152}Eu source was placed before the experiment at the target position in the scattering chamber of the AFRODITE clover array to calibrate the HPGe clover detectors. The γ -ray spectrum collected from the source by the clover detectors was analyzed using MIDAS MTsort software. The auto calibration option of MIDAS MTsort was used to get the gain and offset calibration coefficients. The auto calibration option produced the gain and offset calibration by identifying the known peaks of the ^{152}Eu spectrum and fitting using the polynomial of degree one. Then the gain and offset calibration coefficients were inserted on the MTsort sorting code to produce one-on-one calibrated γ -ray spectrum.

4.1.3 Silicon Detector Energy Calibration and Particle Energy Loss

The ^{226}Ra alpha source was placed at the center of the scattering chamber to calibrate the 24 rings and 32 sectors of S3 silicon detector, while the scattering chamber was vacuumed. The first peak of the alpha source spectrum was selected to calibrate the rings and sectors. The gain and offset calibration coefficients were precisely calculated using the elastic peaks, which were calculated using the kinetic collision kinematics, and SRIM stopping-powers. SRIM

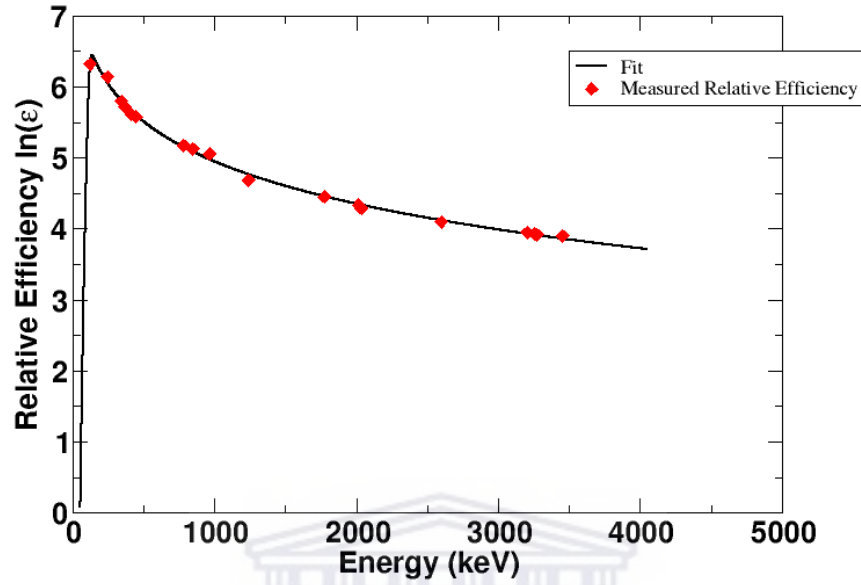


Figure 4.3: Relative efficiency curve.

stopping-powers are calculated using,

$$-\frac{dE}{dx} = \left(\frac{Z_p e^2}{4\pi\epsilon_0} \right)^2 \left(\frac{4\pi Z_t \rho_t N_A}{A_t M_e v^2} \right) \left[\ln\left(\frac{2M_e v^2}{I_E} \right) - \ln(1 - \beta^2) - \beta^2 \right], \quad (4.4)$$

where A_t and ρ_t are the nuclear mass and density of the target material, respectively. $I_E \approx 11Z_t \text{ eV}$ is the mean energy required to ionize an atom of the target material. The SRIM stopping were used to estimate the energy loss of the projectile nuclei through the target.

The gain and offset calibration coefficients were inserted in the MTsort sorting code in order to produce the one-to-one channel-to-energies particle spectrum.

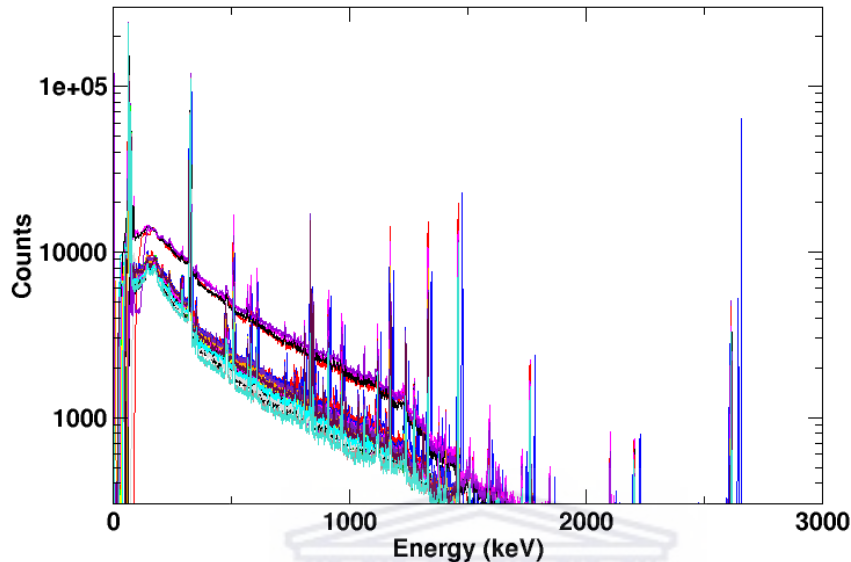


Figure 4.4: All clover spectrum overlapped after calibration.

Figure 4.6 shows some of the uncalibrated and calibrated rings of the S3 silicon detector. The calibrated rings show the trend of the Rutherford scattering, the counts of the rings decrease as the scattering angles increase.

4.2 Background Radiation

Naturally, radiation is everywhere. This is due to a number of several sources that are present in the environment. When detecting radiation it is important to discriminate between the desired radiation from the experiment and the natural occurring radiation. The natural occurring radiation from the environment is called the background radiation. Since in this research work the radiation that is used in analyzing the CERE is of interest, then any other radiation is considered a background radiation. Background radiation is reduced differently for each detector system (S3 silicon and clover detectors).

4.2.1 Broad Particle Energy Gate

Rings and sectors of the S3 silicon detector peak up all kind of charged particles. Ranging from low to high energy particles. The scattered ^{32}S particles are detected in different energies but there are two kinds that are of interest in the CERE experiment, elastic and inelastic particles. The elastic and inelastic peaks are not much separate from each other, considering the fact that the inelastic particle has a recoil energy of about 13% of the beam energy. Particles detected

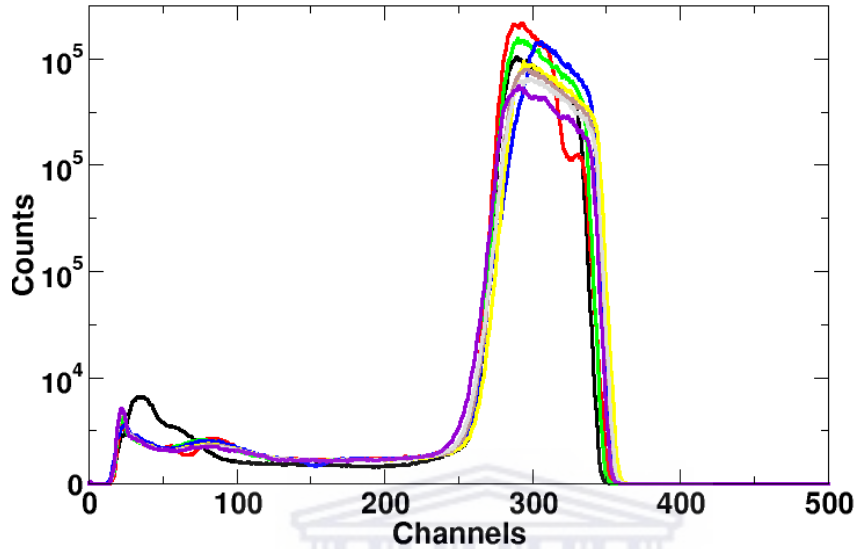


Figure 4.5: First eight uncalibrated rings.

to have energy much less or greater than the elastic particles are considered to be the background radiation. The broad particle energy gate condition is set to subtract such background as shown in Figure 4.9 below.

Figure shows the typical broad energy of the rings. The broad particle energy gate is set at the beginning of the innermost ring and at the end of the outermost ring. This is due to the fact that the innermost ring detects particles with least energies and the outermost ring detects particles with the most energies, as depicted by Figure 4.9 the The radiation that is detected outside of this region is rejected as the background radiation. The same broad particle energy condition is set for the sectors.

4.2.2 Particle Coincidence

Particle spectra background was further subtracted by enforcing particle coincidence condition. The particle coincidence condition is enforced by setting a time gate Δt_p between the adjacent rings and sectors of the S3 silicon detector. This time gate will only allow the particles that are simultaneously detected by both adjacent rings and sectors of the S3 silicon detector.

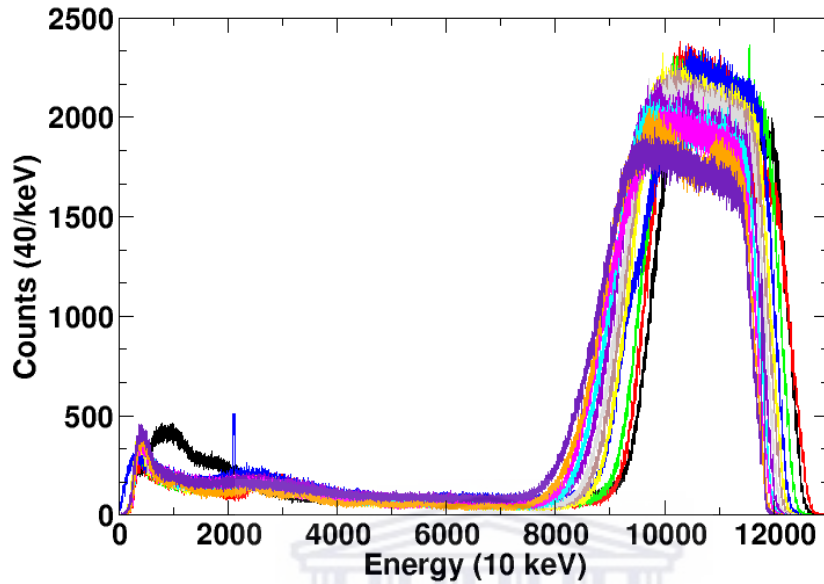


Figure 4.6: First twelve calibrated rings

4.2.3 Particle- γ Coincidence

AFRODITE clover detectors also pick up background radiation. Particle- γ coincidence condition is enforced to separate and reduce further background radiation in the γ -ray spectra for the Doppler correction purposes. This condition requires a simultaneous detection of the particle in the S3 silicon detector and the γ -ray in any of the crystal of the AFRODITE clover array. A time condition spectra $\delta t'$ is recorded of the particle detection in the S3 silicon and the γ ray detection in any of the crystals of the AFRODITE clover array. Anything detected outside the set time gate is discarded for it is considered to be the background radiation.

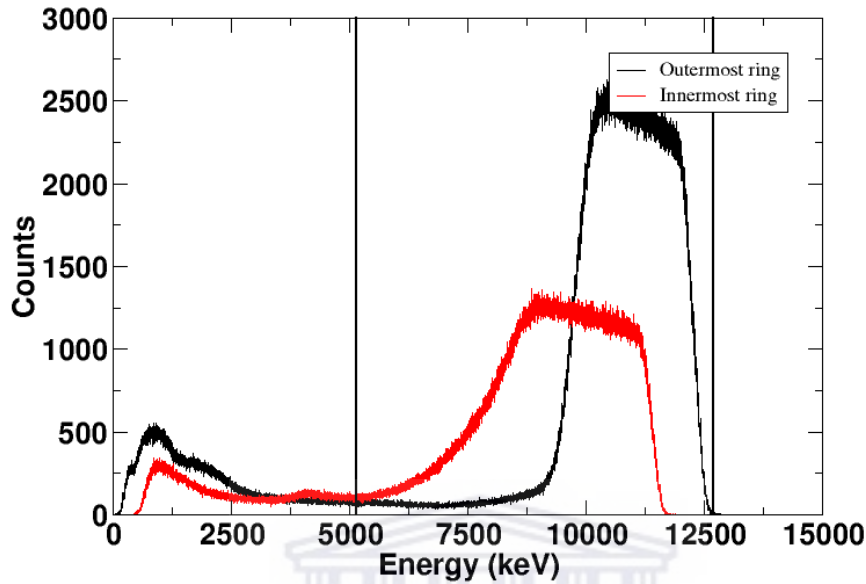


Figure 4.7: Broad particle energy gating.

4.2.4 Energy Difference and Inelastic Conditions

Some of the unwanted background radiation is due to the results of the particle energy deposited on the dead layers of the S3 silicon detector. Energy sharing condition is set to eliminate the unwanted events due to the energy shared between rings, sectors and the dead layers of the S3 silicon detector. The condition $|E_{sector} - E_{ring}|$ is imposed on the data sorting code. $|E_{sector} - E_{ring}|$ is the difference between the energy detected on the ring and the sector. This difference is set to be less than a particular energy which is determined by increasing this energy by steps of 500 keV.

Inelastic condition is a further attempt on allowing only the γ rays that come from the inelastically scattered ^{32}S particles. The condition is set for each of the twenty four rings. The energy from the peak of the ring is cut at the center and from the first cut of the broad particle energy gate condition. γ ray energy from the particle that is detected outside the inelastic condition gate is not used in the Doppler correction calculations. The set of all of the twenty four rings is created and inserted in the sorting code.

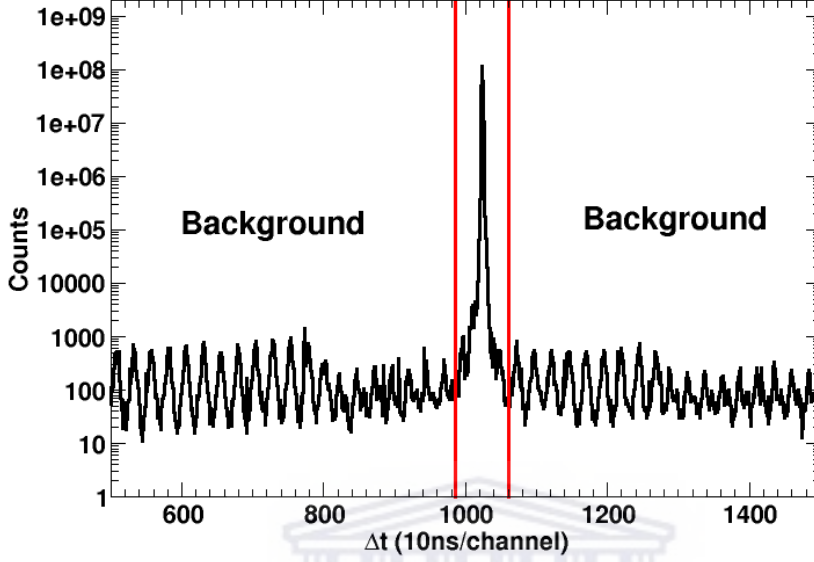


Figure 4.8: Time gates between adjacent rings and sectors.

4.3 Doppler Corrections

The HPGe crystals of the AFRODITE clover array are meant to detect the de-excitation γ -ray photons from both the target and the projectile 2_1^+ excited state. The projectile travels with velocity $v_p \approx 7\%$ of the speed of light c . Its de-excitation γ -ray photon of the 2_1^+ excited state is mostly affected by the Doppler effect phenomenon. This is because the projectile emits γ -ray photons while it's moving and the HPGe crystals of the AFRODITE clover array detect the Doppler shifted γ -ray photons.

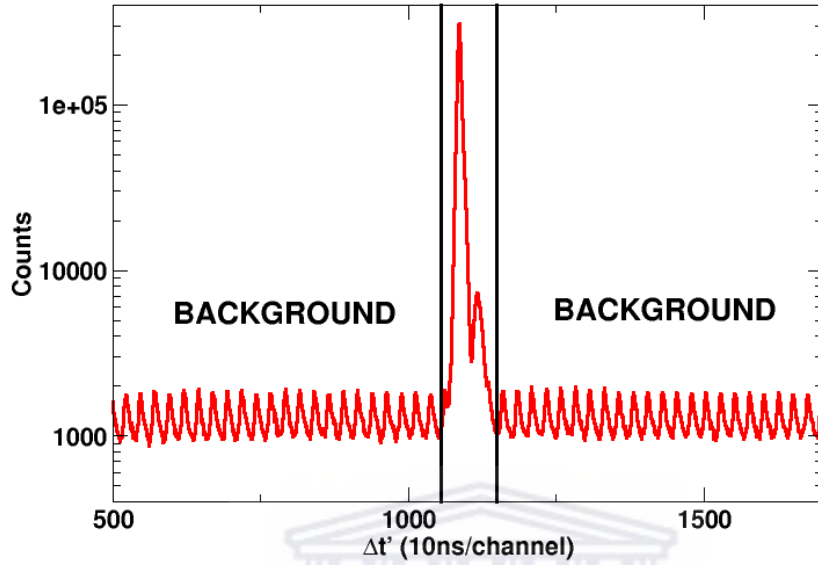
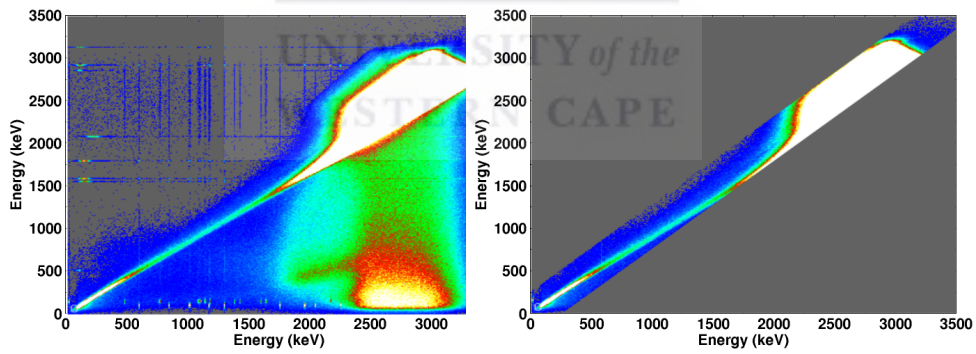
To correct the Doppler shifted γ -ray photons, parameters like the dimensions with respect to the position of the target and projectile, the speed of the moving projectile and the angles of each and every detector involved in the experiment need to be known. Then the Doppler shift equation is used,

$$E_{DS} = E_0 \frac{\sqrt{1 - \beta^2}}{1 - \beta \cos(\theta_{p,\gamma})}, \quad (4.5)$$

where E_{DS} is the Doppler shifted γ -ray energy, E_0 is the emitted γ -ray energy, $\theta_{p,\gamma}$ is the angle between the projectile and the emitted γ -ray and,

$$\beta = \frac{v}{c}, \quad (4.5 \text{ a})$$

and,

Figure 4.9: Particle- γ time condition.

(a) No energy sharing condition

(b) Energy sharing condition

$$\cos(\theta_{p,\gamma}) = \frac{\vec{r}_p \cdot \vec{r}_\gamma}{|r_p| |r_\gamma|}, \quad (4.5 \text{ b})$$

with,

$$x = r \sin\theta \sin\phi, \quad (4.5 \text{ c})$$

$$y = r \sin\theta \cos\phi, \quad (4.5 \text{ d})$$

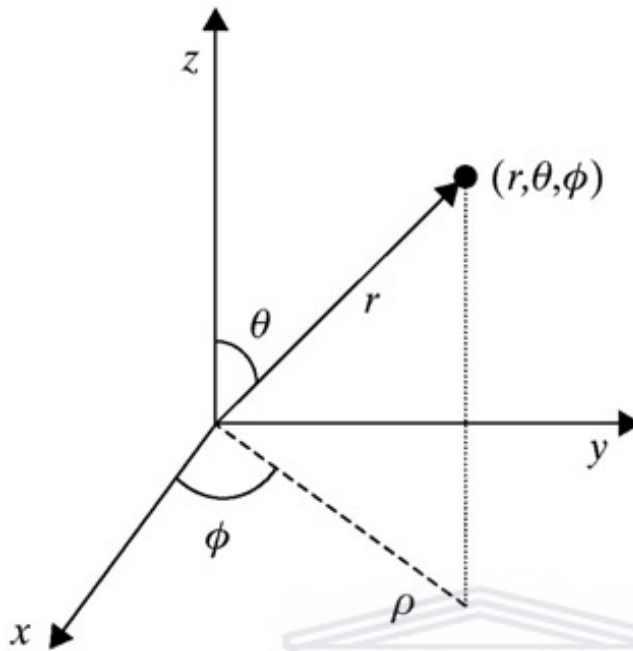


Figure 4.11: Spherical coordinates schematics.

$$z = r \cos \theta, \quad (4.5 \text{ e})$$

then $\cos(\theta_{p,\gamma})$ is,

$$\cos(\theta_{p,\gamma}) = \sin \theta_p \sin \theta_\gamma \cos(\phi_p - \phi_\gamma) + \cos \theta_p \cos \theta_\gamma \quad (4.5 \text{ f})$$

. The Doppler corrected γ -ray energy is corrected using,

$$E_o = E_{DS} \frac{1 - \beta(\sin \theta_p \sin \theta_\gamma \cos(\phi_p - \phi_\gamma) + \cos \theta_p \cos \theta_\gamma)}{\sqrt{1 - \beta^2}}. \quad (4.6)$$

The laboratory angles from the experimental set up were transformed to the angles θ_p and θ_γ .

4.3.1 Background Subtraction and Doppler Corrections

Background radiation data was recorded for both the Doppler shifted and corrected spectra, using the particle- γ coincidence, as shown in Fig. 4.12 and Fig. 4.13, respectively.

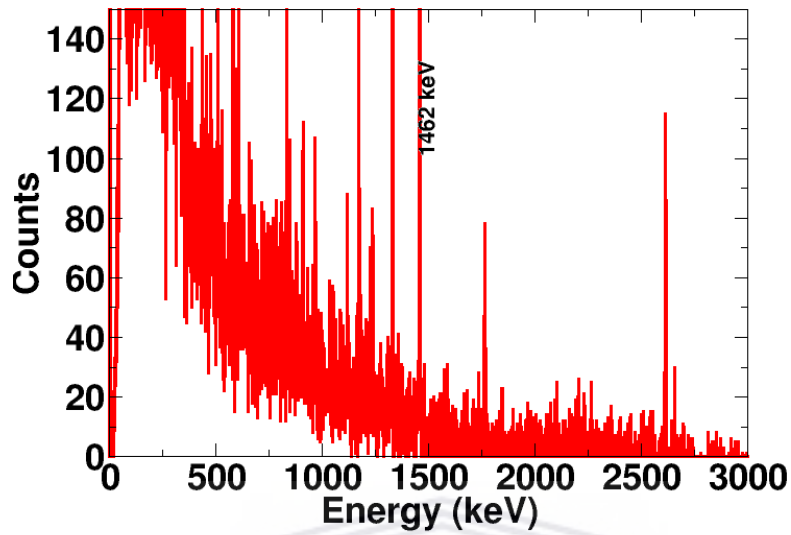


Figure 4.12: Background radiation from the Doppler shifted spectra.

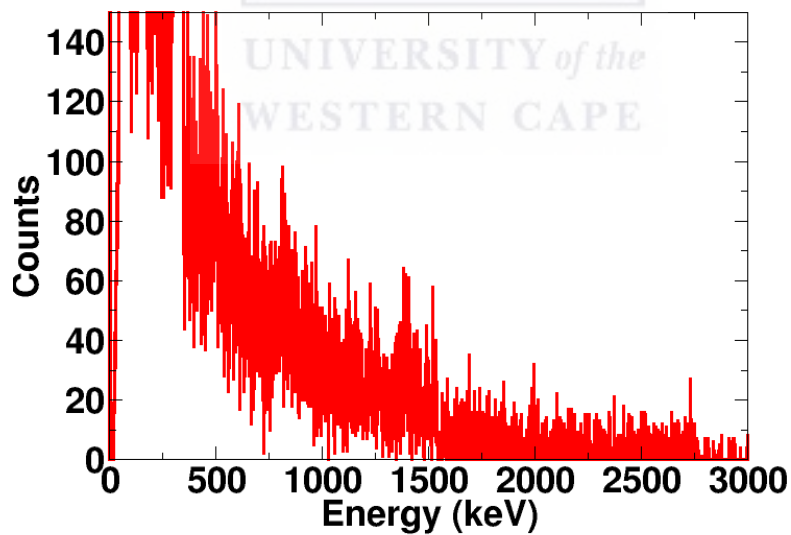


Figure 4.13: Background radiation from the Doppler corrected spectra.

The Doppler shifted and corrected spectra is recorded having the background radiation, as shown in Fig. 4.14 and Fig. 4.15, respectively.

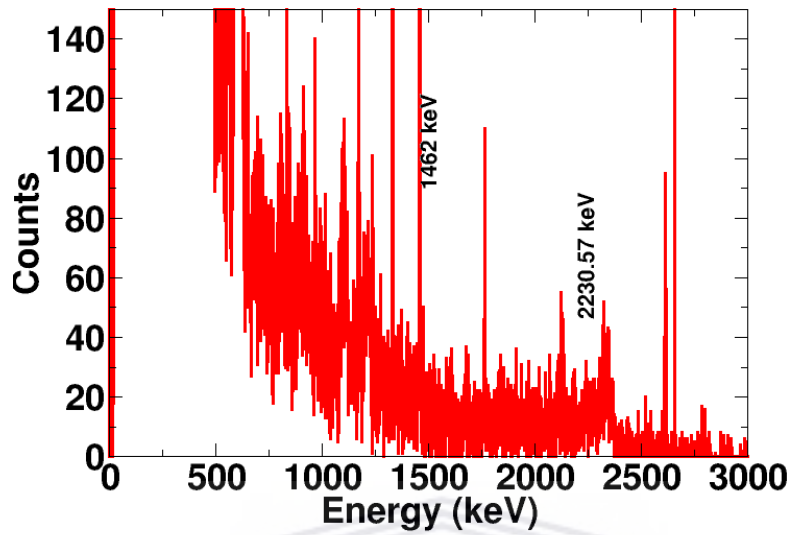


Figure 4.14: Doppler shifted spectra with background radiation.

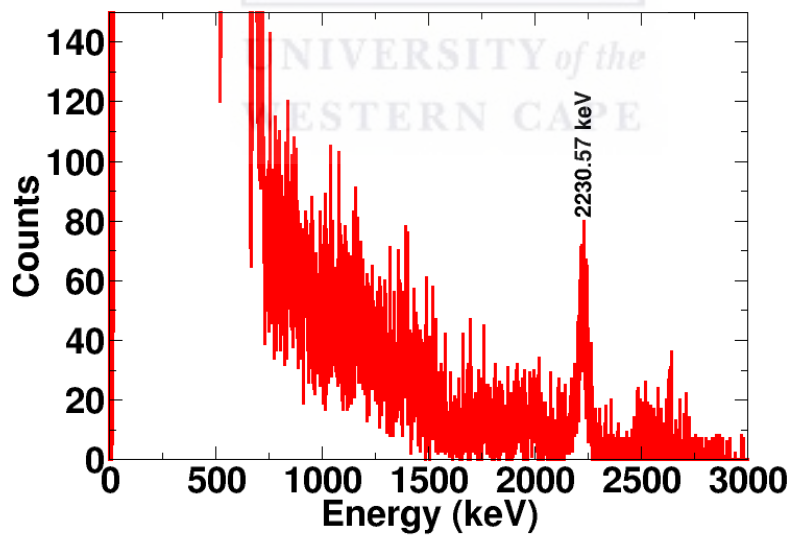


Figure 4.15: Doppler corrected spectra with background radiation.

To eliminate the background radiation from the Doppler shifted and corrected, background radiation from the Doppler shifter in Fig. 4.12 is subtracted from the Doppler shifted spectra with background radiation in Fig. 4.14. The

same procedure is applied to eliminate the background radiation from the Doppler corrected spectra. The resulting Doppler shifted and corrected spectra are shown in Fig. 4.16 and Fig. 4.17, respectively.

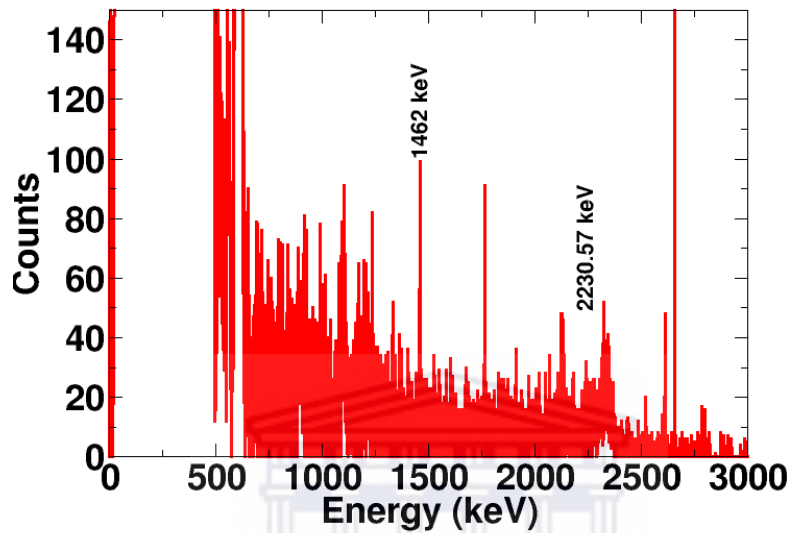


Figure 4.16: Doppler shifted spectra with background radiation subtracted.

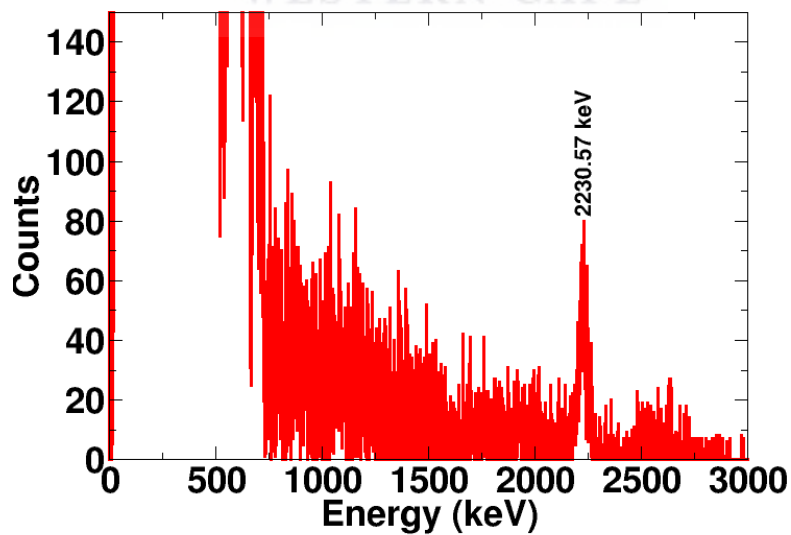


Figure 4.17: Doppler corrected spectra with background radiation subtracted.

The Doppler shifted spectrum in Fig. 4.16 is useful in determining the counts of the ^{194}Pt 's first 2^+ excited state of 328.46(5) keV energy, while the Doppler corrected spectrum in Fig. 4.17 is useful in determining the ^{32}S 's first 2^+ excited state of 2230.56(15) keV energy. The level schemes of ^{32}S and ^{194}Pt showing the ground the ground and some of the excited states, is shown in Fig. 4.18a and Fig. 4.18b.

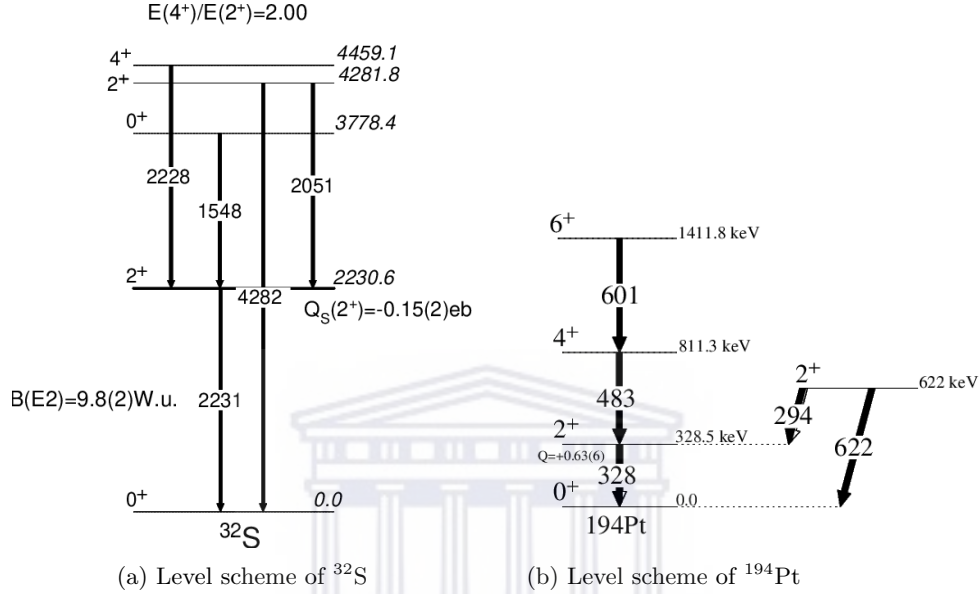


Fig. 4.18a and 4.18b shows low-lying level schemes of ^{32}S and ^{194}Pt with the 2_1^+ excited states at 2230.6 keV and 328.5 keV, respectively.

4.4 GOSIA code and determination of $Q_S(2_1^+)$

The GOSIA code is used to extract electromagnetic matrix elements from the Coulomb excitation data [60]. The extraction of the electromagnetic matrix elements is accomplished by the GOSIA normalization procedure. Projectile de-exciting γ -rays cross-sections are normalized to the target de-exciting γ rays cross-sections. The normalization process is done by fitting the two cross-section by using the transitional $\langle 2_1^+ || E2 || 0_1^+ \rangle$ and diagonal $\langle 2_1^+ || E2 || 2_1^+ \rangle$ matrix elements as the fitting parameters. GOSIA compares the measured γ ray yields from the target nucleus with γ -ray yields from the projectile nucleus.

Target's γ ray yields are related to the projectile's γ ray yields by,

$$\frac{\sigma_{E2}^T W(\theta)^T}{\sigma_{E2}^P W(\theta)^P} = 1.037 \frac{N_\gamma^T \epsilon_\gamma^P}{N_\gamma^P \epsilon_\gamma^T} = \frac{I_\gamma^T}{I_\gamma^P}, \quad (4.7)$$

where σ_{E2}^T and σ_{E2}^P are Coulomb excitation cross section to excite the projectile and nucleus, respectively. $W(\theta)$ is the integrated angular distribution of the de-excited γ rays in coincidence with the inelastic scattered particles. N_γ , ϵ_γ

and I_γ are the measure counts, efficiency and intensity of the de-exciting γ rays. The exponent P and T indicate the projectile and target, respectively. The factor 1.037 represent the 96.45% target enrichment.

Two GOSIA input files were created, one for the target excitation and the other for the projectile excitation. The GOSIA files were used to calculate the γ ray yields, $\sigma_{E2}W(\theta)$ for both the target and the projectile. The normalization procedure of the γ ray yields in ^{32}S to the well known matrix elements in in the target nucleus ^{194}Pt is used to determine the diagonal matrix element of interest ($\langle 2_1^+ || E2 || 2_1^+ \rangle$) in ^{32}S . Where,

$$Q_S(2_1^+) = 0.75793 \langle 2_1^+ || E2 || 2_1^+ \rangle. \quad (4.8)$$

The γ ray yields calculated using Eq. 4.7 for ^{32}S are $\sigma_{E2}^P W(\theta)^P = 4.15938$. Where $N_\gamma^P = 2991.52$, $N_\gamma^T = 2008624.62$, $\epsilon_\gamma^P = 69.79$, $\epsilon_\gamma^T = 335.69$ and γ ray yields for the target $\sigma_{E2}^T W(\theta)^T = 606.101$. The GOSIA input file for the projectile was then used to produce the γ yields calculated by Eq. 4.7 by fixing the values of diagonal matrix element, $\langle 2_1^+ || E2 || 2_1^+ \rangle = [-0.4, +0.4]$ by steps of 0.05 eb. For each of the value of $\langle 2_1^+ || E2 || 0_1^+ \rangle$ the value of the transitional matrix element was determined which produces $\sigma_{E2}^P W(\theta)^P = 4.15938$. The values of were plotted in the $\langle 2_1^+ || E2 || 2_1^+ \rangle - \langle 2_1^+ || E2 || 0_1^+ \rangle$ plane.

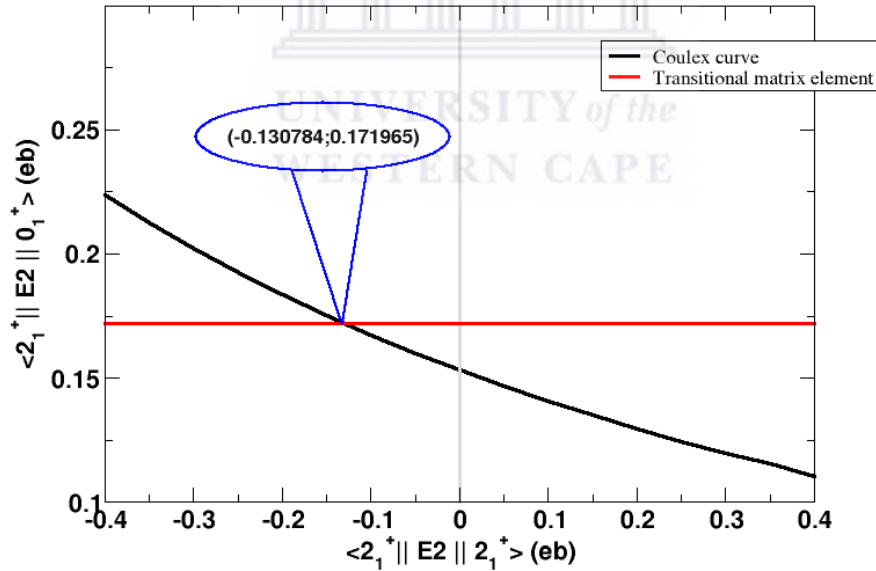


Figure 4.19: $\langle 2_1^+ || E2 || 2_1^+ \rangle - \langle 2_1^+ || E2 || 0_1^+ \rangle$ plane.

The graph shows the change of $\langle 2_1^+ || E2 || 0_1^+ \rangle$ as a function of $\langle 2_1^+ || E2 || 2_1^+ \rangle$ in ^{32}S . The vertical gray line is the reference line between the negative and positive values of $\langle 2_1^+ || E2 || 2_1^+ \rangle$. The horizontal red line is the transitional matrix element $\langle 2_1^+ || E2 || 0_1^+ \rangle = 0.172$ eb. The value is calculated from the ^{32}S life-time measurements, $B(E2) = 9.80(22)$ eb[61]. The intersection of the transitional matrix element and the Coulomb excitation curve at $(-0.130784; 0.171965)$ leads to the extracting of the diagonal matrix element. At this intersection the value of $\langle 2_1^+ || E2 || 2_1^+ \rangle = -0.131$ eb is obtained. Using Eq. 4.8, the spectroscopic quadrupole moment of the first 2^+ state is, $Q_S(2_1^+) = -0.099$ eb.

Error in the extracted $\langle 2_1^+ || E2 || 2_1^+ \rangle$, comes from the errors in the parameters of equation 10. Parameters of equation 10 have error percentage of, N_γ^P (5.11%), N_γ^T (7.86%), ϵ_γ^P (2%), ϵ_γ^T (3%) and $\sigma_{E2}W(\theta)^T$ (2.39%). The error percentage in $\sigma_{E2}W(\theta)^P$ is calculated using error propagation method and is to be 9.37%. The upper and lower limits of $\sigma_{E2}W(\theta)^P$ due to the error percentage, was determined by adding and subtracting the error in $\sigma_{E2}W(\theta)^P$. Two more Coulomb excitation curves of $\langle 2_1^+ || E2 || 2_1^+ \rangle - \langle 2_1^+ || E2 || 0_1^+ \rangle$ values that correspond to the upper and lower limits of $\sigma_{E2}W(\theta)^P$ are plotted.

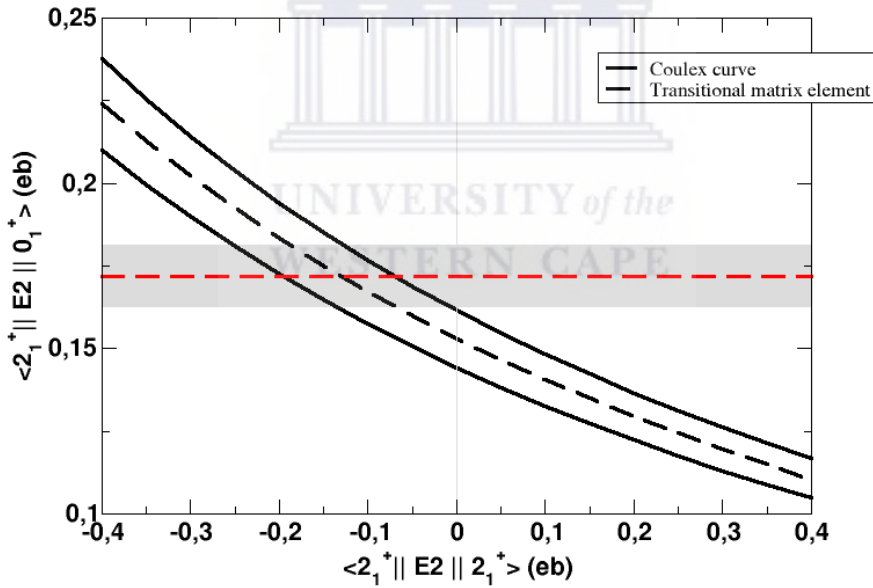


Figure 4.20: $\langle 2_1^+ || E2 || 2_1^+ \rangle - \langle 2_1^+ || E2 || 0_1^+ \rangle$ plane with error bands.

The Coulomb excitation curve is represented by the black dotted line with its 1- σ limits which are represented by the two black solid lines. The transitional matrix element, $\langle 2_1^+ || E2 || 0_1^+ \rangle = 0.172$ eb, is represented by the red dotted line with its 1- σ limits represented by the red solid lines. Assuming that there is no uncertainty in $\langle 2_1^+ || E2 || 0_1^+ \rangle$, the intersection in the line $\langle 2_1^+ || E2 || 0_1^+ \rangle = 0.172$ eb and the 1- σ limits of the Coulomb excitation curve gives the uncertainty of

± 0.062 *eb* in $\langle 2_1^+ || E2 || 2_1^+ \rangle$. Similarly, assuming that there is no uncertainty in the Coulomb excitation curve, the intersection of the Coulomb excitation and the life-time measurement's $1-\sigma$ limits gives the uncertainty of ± 0.064 *eb* in $\langle 2_1^+ || E2 || 0_1^+ \rangle$. Adding these two errors in quadrature results in ± 0.090 *eb*. The full reading of the measured diagonal matrix element of ^{32}S is $\langle 2_1^+ || E2 || 2_1^+ \rangle = -0.131 \pm 0.090$ *eb*. Using Eq. 4.8, a value of $Q_S(2_1^+) = -0.099 \pm 0.068$ *eb* is obtained via Coulomb excitation reorientation effect.



Chapter 5

Discussion and Conclusions

5.1 Discussion

The CE experiment of $^{194}\text{Pt}(^{32}\text{S}, ^{32}\text{S}^*)^{194}\text{Pt}^*$ with “safe” beam energy, $E_p=120.3$ MeV. The energy was because it is less than the Coulomb barrier, i.e $E_{Cb}=163.97$ MeV, and it provided minimum safe distance between nuclear surface of $S_{min} = 6.5$ fm, as suggested by Spear *et al.* Rutherford scattering pattern is typically shown by the particle energy detected by the first twelve rings in Fig. 4.6. This serves as the experimental confirmation of the “safe” $E_p=120.3$ beam energy. Moreover, this “safe” bombarding energy was able to provide the semi-classical approach for this CE experiment. The semi-classical approach was validated by the Sommerfeld parameter $\eta=143$, which is much greater than one as the semi-classical approach requires. The ratio $\frac{\Delta E}{E_{cm}}=0.025$ led to the adiabaticity parameter ξ , which is shown to be satisfied by Fig. 3.2. These pivotal requirements served as a judgment for the appropriate CE experiment and they were all valid for this CE experiment.

The data collected from the AFRODITE clover array coupled with the S3 silicon detector was well calibrated. Efficiency calibration was observed by the fitting of the γ -ray efficiencies from the ^{152}Eu and ^{56}Co sources to the efficiency curve by Eq. 4.3. The ^{56}Co source was used to compensate the efficiency of detecting γ -rays from the de-excitation of the ^{32}S from the first 2^+ excited state. Energy calibration of the clover detectors played a pivotal role in Doppler correction calculations. The iThemba LABS’ AFRODITE clover array coupled with the S3 silicon detector provided satisfying results in background subtraction, which was done through the coincidence conditions, and Doppler correction calculations as shown in Fig. 4.17.

The prolate shape, $Q_S(2_1^+) = -0.099 \pm 0.068$ eb, determined in this work contradicts modern beyond mean-field calculations [62], which as shown in the top panel of Fig. 5.1, predict oblate shapes for the ground and first excitations, and the simple pairing coupling scheme [63]. According to the latter, prolate shapes are expected at the beginning of the *sd* shell as particles start filling up the empty shells, whereas an expected flip over to oblate shapes is expected at around mid-shell, when it is more appropriate to talk about holes in the

filled shell, which align their orbits along the polar axis, hence leading to oblate shapes. The mystery of the shape of nucleus at low excitation remains and the reason may lie on the formation of cluster structures. In fact, the second super-deformed band in ^{40}Ca is expected to arise from the ^{32}S core coupled to 8 particle - 8 hole excitations, i. e., ^{32}S core + two alpha particles [64]. This could be indicated by the relatively higher excitation energies calculated by the beyond mean-field model, as shown in the bottom panel of Fig. 5.1. Finally, against predictions shown in Fig. 5.1, no super-deformed band has yet been discovered in ^{32}S .

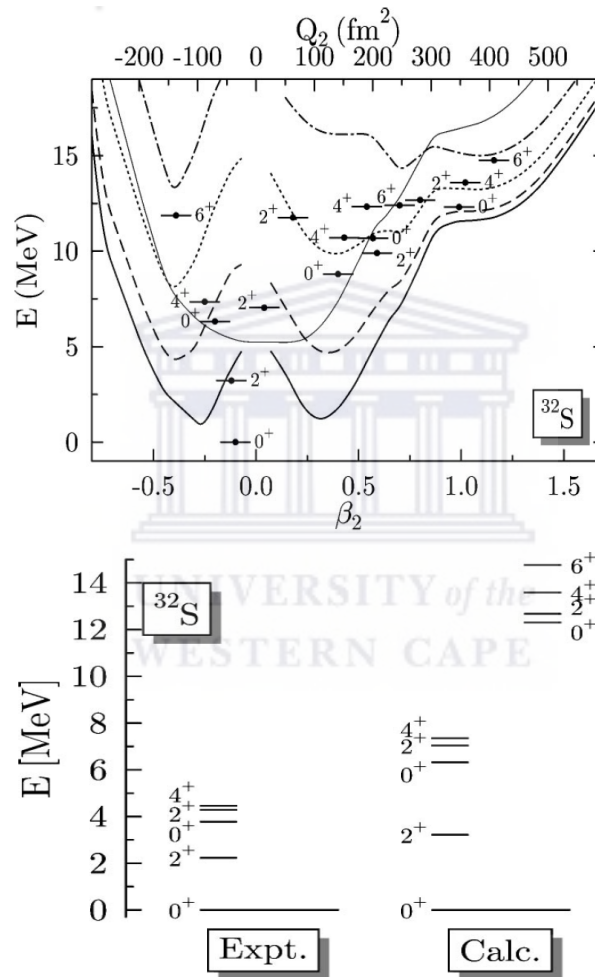


Figure 5.1: (Top panel) Deformation energy curves for $J = 0, 2, 4,$ and 6 corresponding to thick solid, dashed, dotted, and dash-dotted lines, respectively [62]. (Bottom panel) Comparison of experimental (left) and calculated (right) excitation energies of even spin and positive parity states in ^{32}S [62].

5.2 Conclusion

The Coulomb excitation reorientation effect experiment of $^{194}\text{Pt}(^{32}\text{S}, ^{32}\text{S}^*)^{194}\text{Pt}^*$ was performed at iThemba LABS' AFRODITE clover array coupled with the S3 silicon detector at safe bombarding energies. The reaction was a semi-classical approach validated by the Sommerfeld and adiabaticity parameter. The counts from the well Doppler corrected peak of ^{32}S excitation and from the uncorrected peak of ^{194}Pt excitation, were used in GOSIA calculations to determine the diagonal matrix element of the first 2^+ excited state in ^{32}S . GOSIA calculations resulted in $\langle 2_1^+ || E2 || 2_1^+ \rangle = -0.131 \pm 0.090$ *eb*, in which yielded $Q_S(2_1^+) = -0.099 \pm 0.068$ *eb*. This CERE experiment yields a prolate shape for the first 2^+ excited state of ^{32}S in the intrinsic frame of the nucleus, in agreement with the zig zag of shapes previously found at the end of the *sd* shell, but in disagreement with old and modern theoretical calculations.



Appendix A

AFRODITE detector angles

A.1 AFRODITE clover angle

Clover	$\theta(^{\circ})$	$\phi(^{\circ})$
1	90	90
2	90	45
3	90	225
4	90	315
5	135	0
6	135	270
7	135	45
8	90	270

Table A.1: AFRODITE clover angles

A.2 Clover crystal angles

Crystal	$\theta(^{\circ})$	$\phi(^{\circ})$
Crystal 1 A	84.80	95.11
Crystal 2 A	84.80	49.85
Crystal 3 A	84.80	230.33
Crystal 4 A	84.80	320.28
Crystal 5 A	130.06	5.16
Crystal 6 A	130.06	275.02
Crystal 7 A	130.06	49.85
Crystal 8 A	84.80	275.02
Crystal 1 B	95.11	95.11
Crystal 2 B	95.11	49.85
Crystal 3 B	95.11	230.33
Crystal 4 B	95.11	320.28
Crystal 5 B	140.37	5.12
Crystal 6 B	140.37	275.02
Crystal 7 B	140.37	49.85
Crystal 8 B	95.11	275.02
Crystal 1 C	95.11	84.80
Crystal 2 C	95.11	39.53
Crystal 3 C	95.11	220.02
Crystal 4 C	95.11	309.97
Crystal 5 C	140.37	354.66
Crystal 6 C	140.37	264.71
Crystal 7 C	140.37	39.53
Crystal 8 C	95.11	264.71
Crystal 1 D	84.80	84.80
Crystal 2 D	84.80	39.53
Crystal 3 D	84.80	220.02
Crystal 4 D	84.80	309.97
Crystal 5 D	130.06	354.66
Crystal 6 D	130.06	264.71
Crystal 7 D	130.06	39.53
Crystal 8 D	84.80	264.71

Table A.2: AFRODITE crystal angles

Appendix B

S3 Silicon detector dimensions



B.1 S3 Silicon Detector ring radii and average scattering angles

Ring	r_{min} (mm)	r_{max} (mm)	Average scattering angle ($^{\circ}$)
1	11.48	12.366	110.59
2	12.466	13.352	111.14
3	13.452	14.338	111.73
4	14.438	15.324	112.34
5	15.424	16.31	112.97
6	16.41	17.296	113.66
7	17.396	18.282	114.38
8	18.382	19.268	115.15
9	19.368	20.254	115.96
10	20.354	21.24	116.81
11	21.34	22.226	117.73
12	22.326	23.212	118.70
13	23.312	24.198	119.73
14	24.298	25.184	120.84
15	25.284	26.17	122.02
16	26.27	27.156	123.28
17	27.256	28.142	124.64
18	28.242	29.128	126.09
19	29.228	30.114	127.66
20	31.2	31.1	129.34
21	31.2	32.086	131.15
22	32.186	33.072	133.04
23	33.172	34.058	135.22
24	34.158	35.044	137.49

Table B.1: S3 silicon detector ring radii

Appendix C

Sorting Code

```
*formats
clover[1:8](e1, e2, e3, e4, x1, x2, x3, x4)
sect[21:52](e1, x1)
ring[53:77](e1, x1)

*data
#####_CLOVER_CALIBRATION_#####

Gainarray segA
1 ( 1.795961 0.4086982 0.000 )
2 ( 2.485065 0.5570451 0.000 )
3 ( 1.461670 0.3891653 0.000 )
4 ( 0.5881280 0.3891652 0.000 )
5 ( 0.8965021 0.3746466 0.000 )
6 ( 1.346537 0.3733864 0.000 )
7 ( 2.137347 0.5696860 0.000 )
8 ( 0.6964304 0.3683980 0.000 )
9 (-2.799365301 0.5913063004 0.000 )

Gainarray segB
1 ( 0.6868676 0.3814872 0.000 )
2 ( 0.2021003 0.5389180 0.000 )
3 ( 0.2490826 0.3713361 0.000 )
4 ( 1.042676 0.3936636 0.000 )
5 ( 1.084525 0.3800091 0.000 )
6 ( 0.7687070 0.3731689 0.000 )
7 ( 1.968461 0.5414200 0.000 )
8 ( 0.9218031 0.3829675 0.000 )
9 (-1.775311027 0.5634454792 0.000 )

Gainarray segC
1 ( 1.823216 0.4138062 0.000 )
2 ( 0.8996830 0.3775201 0.000 )
3 ( 0.178840 0.4682673 0.000 )
4 ( 1.29505 0.5611275 0.000 )
5 ( 0.8536258 0.3600876 0.000 )
6 ( 0.6643982 0.1622458 0.000 )
7 ( 0.9362671 0.3560432 0.000 )
8 ( 1.137618 0.5899740 0.000 )
9 (-1.7542247326 0.5345007943 0.000 )

Gainarray segD
1 ( 1.919427 0.4142190 0.000 )
2 ( 3.072040 0.4237383 0.000 )
3 ( 1.014185 0.4001911 0.000 )
4 ( 0.9489753 0.5399461 0.000 )
5 ( 1.222456 0.3609516 0.000 )
6 ( 0.8301001 0.3632125 0.000 )
7 ( 1.352486 0.5252028 0.000 )
8 ( 0.74952564 0.3583033 0.000 )
9 (-0.8437037504 0.363687404 0.000 )

#####_RING_AND SECTOR_CALIBRATION_#####

Gainarray ring
53 (-445.14 37.59 0.000)
54 (-399.97 37.17 0.000)
55 (-414.40 36.73 0.000)
56 (-518.84 36.16 0.000)
57 (-390.93 35.21 0.000)
58 (-380.62 35.27 0.000)
59 (-362.09 35.01 0.000)
60 (-358.27 35.10 0.000)
61 (-331.41 34.34 0.000)
62 (-304.06 33.58 0.000)
63 (-302.34 33.35 0.000)
64 (-311.15 32.74 0.000)
65 (-294.91 33.02 0.000)
66 (-301.71 32.74 0.000)
```



```

67 (-289.92 32.79 0.000)
68 (-292.32 31.68 0.000)
69 (-290.70 31.87 0.000)
70 (-284.70 32.41 0.000)
71 (-261.66 32.46 0.000)
72 (-260.20 32.40 0.000)
73 (-254.69 32.53 0.000)
74 (-240.46 31.28 0.000)
75 (-233.53 31.19 0.000)
76 (-251.20 31.64 0.000)
77 (0.00 0.00 0.000)

```

```

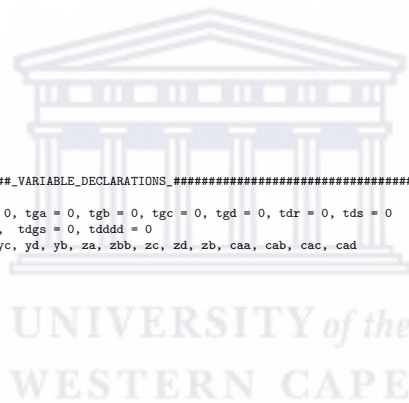
Gainarray sect
21 (-469.76 12.36 0.000)
22 (-466.78 12.37 0.000)
23 (-438.47 12.42 0.000)
24 (-451.13 12.30 0.000)
25 (-448.22 12.14 0.000)
26 (-448.77 12.21 0.000)
27 (-450.28 12.03 0.000)
28 (-418.28 12.01 0.000)
29 (-442.23 12.03 0.000)
30 (-441.63 12.31 0.000)
31 (-440.80 12.41 0.000)
32 (-436.12 12.29 0.000)
33 (-500.12 12.29 0.000)
34 (-470.11 12.55 0.000)
35 (-462.53 12.68 0.000)
36 (-472.54 13.01 0.000)
37 (-455.52 12.17 0.000)
38 (-461.78 12.27 0.000)
39 (-463.92 12.23 0.000)
40 (-476.12 12.34 0.000)
41 (-476.21 12.57 0.000)
42 (-482.67 12.45 0.000)
43 (-492.50 12.88 0.000)
44 (-539.90 13.01 0.000)
45 (-491.35 12.50 0.000)
46 (-498.53 12.74 0.000)
47 (-505.06 13.03 0.000)
48 (-498.19 13.02 0.000)
49 (-496.14 12.68 0.000)
50 (-484.65 12.52 0.000)
51 (-479.50 12.31 0.000)
52 (0.00 0.00 0.000)

```

```

#####_VARIABLE_DECLARATIONS_#####
longlong ngg
longlong tg = 0, ts = 0, tr = 0, td = 0, tga = 0, tgb = 0, tgc = 0, tgd = 0, tdr = 0, tds = 0
longlong tss1 = 0, trr1 = 0, tdgr = 0, tdgs = 0, tdddd = 0
float xa, xbb, xc, xd, xb, ya, ybb, yc, yd, yb, za, zbb, zc, zd, zb, caa, cab, cac, cad
valuearray tg1[1:8]
0 0 0 0 0 0 0 0
valuearray energyg1[1:8]
0 0 0 0 0 0 0 0
valuearray tg2[1:8]
0 0 0 0 0 0 0 0
valuearray energyg2[1:8]
0 0 0 0 0 0 0 0
valuearray tg3[1:8]
0 0 0 0 0 0 0 0
valuearray energyg3[1:8]
0 0 0 0 0 0 0 0
valuearray tg4[1:8]
0 0 0 0 0 0 0 0
valuearray energyg4[1:8]
0 0 0 0 0 0 0 0
valuearray sum[1:8]
0 0 0 0 0 0 0 0
valuearray nrr[1:24]
0 0 0 0 0 0 0 0
0 0 0 0 0 0 0 0
0 0 0 0 0 0 0 0
0 0 0 0 0 0 0 0
valuearray nss[1:32]
0 0 0 0 0 0 0 0
0 0 0 0 0 0 0 0
0 0 0 0 0 0 0 0
0 0 0 0 0 0 0 0
0 0 0 0 0 0 0 0
valuearray energyr[1:24]
0 0 0 0 0 0 0 0
0 0 0 0 0 0 0 0
0 0 0 0 0 0 0 0
0 0 0 0 0 0 0 0
valuearray energys[1:32]
0 0 0 0 0 0 0 0
0 0 0 0 0 0 0 0
0 0 0 0 0 0 0 0
0 0 0 0 0 0 0 0
valuearray tr1[1:24]
0 0 0 0 0 0 0 0
0 0 0 0 0 0 0 0
0 0 0 0 0 0 0 0
0 0 0 0 0 0 0 0
valuearray ts1[1:32]
0 0 0 0 0 0 0 0
0 0 0 0 0 0 0 0
0 0 0 0 0 0 0 0
0 0 0 0 0 0 0 0
0 0 0 0 0 0 0 0
valuearray sundop[1:8]
0 0 0 0 0 0 0 0
valuearray sundopx[1:8]

```



```

0 0 0 0 0 0 0
valuearray sumnodop[1:8]
0 0 0 0 0 0 0
valuearray sumnodopx[1:8]
0 0 0 0 0 0 0
valuearray e1ica[1:8]
0 0 0 0 0 0 0
valuearray e1icb[1:8]
0 0 0 0 0 0 0
valuearray e1icc[1:8]
0 0 0 0 0 0 0
valuearray e1icd[1:8]
0 0 0 0 0 0 0
valuearray x_1[1:8]
0 0 0 0 0 0 0
valuearray x_2[1:8]
0 0 0 0 0 0 0
valuearray x_3[1:8]
0 0 0 0 0 0 0
valuearray x_4[1:8]
0 0 0 0 0 0 0
valuearray y_1[1:8]
0 0 0 0 0 0 0
valuearray y_2[1:8]
0 0 0 0 0 0 0
valuearray y_3[1:8]
0 0 0 0 0 0 0
valuearray y_4[1:8]
0 0 0 0 0 0 0
valuearray z_1[1:8]
0 0 0 0 0 0 0
valuearray z_2[1:8]
0 0 0 0 0 0 0
valuearray z_3[1:8]
0 0 0 0 0 0 0
valuearray z_4[1:8]
0 0 0 0 0 0 0
valuearray sumdr[1:24]
0 0 0 0 0 0 0
0 0 0 0 0 0 0
0 0 0 0 0 0 0
valuearray sumdr[1:24]
0 0 0 0 0 0 0
0 0 0 0 0 0 0
0 0 0 0 0 0 0
valuearray sumdrab[1:24]
0 0 0 0 0 0 0
0 0 0 0 0 0 0
0 0 0 0 0 0 0
0 0 0 0 0 0 0
valuearray eegdop[1:9]
0 0 0 0 0 0 0 0 0
float pi = 3.14

!#####_DETECTOR_DISTANCES_FROM_TARGET_#####

float d_target2ge = 19.60, d_target2s3 = -1.30

!#####_THETA_ANGLE_OF_CLOVERS_#####

valuearray ge_theta[1:8]
1.57080 1.57080 1.57080 1.57080 2.35620 2.35620 2.35620 1.57080

!#####_PHI_ANGLE_OF_CLOVERS_#####

valuearray ge_phi[1:8]
1.57080 0.78540 3.92700 5.49779 0.00000 4.71239 0.78540 4.71239

!#####_THETA_ANGLE_OF_RINGS_#####

valuearray angdis[1:24]
2.39969 2.36 2.3232 2.28908 2.25743 2.22805
2.20074 2.17534 2.15168 2.12961 2.10899 2.08971
2.07164 2.05469 2.03877 2.0238 2.00969 1.99638
1.98381 1.97192 1.96067 1.94999 1.93986 1.93024

!#####_BETA_#####

valuearray beta[1:24]
0.0672633371 0.0675699514 0.0678668388 0.0681527568 0.0684269653 0.0686891111
0.0689391314 0.0691771756 0.0694035433 0.0696186364 0.0698229222 0.0700169062
0.0702011115 0.0703760643 0.0705422833 0.0707002723 0.0708505161 0.0709934766
0.0711295921 0.071259276 0.0713829171 0.0715088 0.071613506 0.0712114
!#####_PHI_ANGLE_OF_SECTORS_#####

!valuearray sec_phi[1:32]
!3.3379421944 3.1415926536 2.9452431127 2.7488935719 2.552544031 2.3561944902 2.1598449493 1.9634954085
!1.7671458676 1.5707963268 1.3744467859 1.1780972451 0.9817477042 0.7853981634 0.5890486225 0.3926990817
!0.1963495408 6.2831853072 6.0868357663 5.8904862255 5.6941366846 5.4977871438 5.3014376029 5.1050880621
!4.9087385212 4.7123889804 4.5160394395 4.3196898987 4.1233403578 3.926990817 3.7306412761 3.5342917353

valuearray sec_phi[1:32]
0.09817 0.29452 0.49087 0.68722 0.88357 1.07992 1.27627 1.47262
1.66897 1.86532 2.06167 2.25802 2.45437 2.65072 2.84707 3.04342
3.23977 3.43612 3.63247 3.82882 4.02516 4.22152 4.41786 4.61421
4.81056 5.00691 5.20326 5.39961 5.59596 5.79231 5.98866 6.18501

!#####_THETA_ANGLE_OF_CRYSTALS_#####

valuearray crys_a_theta[1:8]

```



```

1.48 1.48 1.48 1.48 2.27 2.27 2.27 1.48
valuearray crys_b_theta[1:8]
1.66 1.66 1.66 1.66 2.45 2.45 2.45 1.66
valuearray crys_c_theta[1:8]
1.66 1.66 1.66 1.66 2.45 2.45 2.45 1.66
valuearray crys_d_theta[1:8]
1.48 1.48 1.48 1.48 2.27 2.27 2.27 1.48

!#####_PHI_ANGLE_OF_CRISTALS_#####

valuearray crys_a_phi[1:8]
1.66 0.87 4.02 5.59 0.09 4.80 0.87 4.80
valuearray crys_b_phi[1:8]
1.66 0.87 4.02 5.59 0.09 4.80 0.87 4.80
valuearray crys_c_phi[1:8]
1.48 0.69 3.84 5.41 6.19 4.62 0.69 4.62
valuearray crys_d_phi[1:8]
1.48 0.69 3.84 5.41 6.19 4.62 0.69 4.62

!#####_INELASTIC_GATES_#####

valuearray inelas_max[1:24]
10907 10873 10871 10569 10588 10519
10419 10351 10290 10231 10137 10069
10010 9925 9871 9499 9866 9929
9722 9625 9575 9464 9482 9404
valuearray inelas_min[1:24]
5141 5141 5141 5141 5141 5141
5141 5141 5141 5141 5141 5141
5141 5141 5141 5141 5141 5141
5141 5141 5141 5141 5141 5141

*spectra
!#####_SPECTRUM_DEFINITIONS_#####

!rclovera: gamma spectra for crystal a
!rcloverb: gamma spectra for crystal b
!rcloverc: gamma spectra for crystal c
!rcloverd: gamma spectra for crystal d
!sectors: particle energy spectra for sectors
!ring:particle energy spectra for sectors
!hitpatg: hitpattern for Ge detectors
!hitpatr: hitpattern for rings
!hitpats: hitpattern for sectors
!timesi: ring and time difference spectrum
!timeg1: ring and gamma time difference spectrum
!timeg2: sector and gamma time difference spectrum
!ge_sum_no_dopplerr: non Doppler corrected gamma spectra for individual rings and all clovers (after conditions)
!ge_sum_no_doppler: non Doppler corrected gamma spectra for all rings and all clovers (after conditions)
!ge_sum_no_doppler2: non Doppler corrected gamma spectra for individual rings (after conditions)
!ge_sum_dopplerr: Doppler corrected gamma spectra for individual rings and all clovers (after conditions)
!ge_sum_doppler: Doppler corrected gamma spectra for all rings and all clovers (after conditions)
!ge_sum_doppler2: Doppler corrected gamma spectra for individual rings (after conditions)
!ge_sum_doppler2: Doppler corrected gamma spectra for all rings (after conditions)
!ge_sum_doppleraddb[1:24]: Doppler corrected gamma spectra for each ring (after conditions)
!ge_sum_doppleraddb: add back Doppler corrected gamma spectra for all rings (after conditions)
!2D ring-gamma histogram (ring-gamma time difference (x-axis) & sum of all clover energies (y-axis))
!2D sector-gamma histogram (sector-gamma time difference (x-axis) & sum of all clover energies (y-axis))
! : 2d si matrix (sector energy (x axis) & ring energy (y axis))

rclovera[1:8] 5000
rcloverb[1:8] 5000
rcloverc[1:8] 5000
rcloverd[1:8] 5000
sectors[1:32] 65536
rings[1:24] 65536
hitpatg 108 32
hitpatr 108 32
hitpats 64 32
timesi 4096 32
timeg1 4096 32
timeg2 4096 32
ge_sum_no_dopplerr[1:24] 5000 32
ge_sum_no_doppler 5000 32
ge_sum_no_doppler2[1:24] 5000 32
ge_sum_no_doppler2 5000 32
ge_sum_dopplerr[1:24] 5000 32
ge_sum_doppler 5000 32
ge_sum_doppler2[1:24] 5000 32
ge_sum_doppler2 5000 32
ge_sum_doppleraddb[1:24] 5000 32
ge_sum_doppleraddb 5000 32
matdgr 2048 2d
matdgs 2048 2d
si_mat 4096 2d
eeg 4096 32
eegdc 4096 32
si_matdc 4096 2d

*commands
!#####_COMMANDS_#####

doloop i from 1 to 32 step +1
{
  energys(i) = 0
  ts1(i) = 0
}
doloop i from 1 to 24 step +1

```

```

{
  energyr(i) = 0
  tr1(i) = 0
  summdr(i) = 0
  sumdr(i) = 0
  sumdrab(i) = 0
}
doloop i from 1 to 8 step +1
{
  sum(i) = 0
  summodop(i) = 0
  sumdop(i) = 0
  eegdop(i) = 0
  energyg1(i)=0
  tg1(i) = 0
  e11ca(i) = 0
  e11cb(i) = 0
  e11cc(i) = 0
  e11cd(i) = 0
  energyg2(i)=0
  tg2(i) = 0
  x_1(i) = 0
  x_2(i) = 0
  x_3(i) = 0
  x_4(i) = 0
  energyg3(i)=0
  tg3(i) = 0
  y_1(i) = 0
  y_2(i) = 0
  y_3(i) = 0
  y_4(i) = 0
  energyg4(i)=0
  tg4(i) = 0
  z_1(i) = 0
  z_2(i) = 0
  z_3(i) = 0
  z_4(i) = 0
}
ns = 0
nr = 0
nga = 0
ngb = 0
ngc = 0
ngd = 0

createlst glist from clover
createlst slist from sect
createlst rlist from ring

gain glist.e1 segA factor 1.00
gain glist.e2 segB factor 1.00
gain glist.e3 segC factor 1.00
gain glist.e4 segD factor 1.00

loopif $g1=glist.e1 gt 0
{
  g = group($g1)
  inc hitpatg(g)
  energyg1(g)=$g1.e1
  inc rclovera($g1.e1) indexed g
  tg=timestampof($g1.e1)
  tg1(g) = timestampof($g1.e1)
  sum(g) = sum(g) + $g1.e1
  nga = nga + 1
}
loopif $g2=glist.e2 gt 0
{
  g = group($g2)
  inc hitpatg(g)
  energyg2(g)=$g2.e2
  inc rcloverb($g2.e2) indexed g
  tg=timestampof($g2.e2)
  tg2(g) = timestampof($g2.e2)
  sum(g) = sum(g) + $g2.e2
  ngb = ngb + 1
}
loopif $g3=glist.e3 gt 0
{
  g = group($g3)
  inc hitpatg(g)
  energyg3(g)=$g3.e3
  inc rloverc($g3.e3) indexed g
  tg=timestampof($g3.e3)
  tg3(g) = timestampof($g3.e3)
  sum(g) = sum(g) + $g3.e3
  ngc = ngc + 1
}
loopif $g4=glist.e4 gt 0
{
  g = group($g4)
  inc hitpatg(g)
  energyg4(g)=$g4.e4
  inc rloverd($g4.e4) indexed g
  tg=timestampof($g4.e4)
  tg4(g) = timestampof($g4.e4)
  sum(g) = sum(g) + $g4.e4
  ngd = ngd + 1
}
}

```




```

gain slist.e1 sect factor 1.00
gain rlist.e1 ring factor 1.00

!*****_BROAD_ENERGY_GATES_CONDITION_*****

loopif $r=rlist.e1 passes (0.0,65536.0)
{
  g = group($r) - 52
  inc hitpatr(g)
  energyr(g) = $r.e1
  inc rings($r.e1) indexed g
  tr = timestampof($r.e1)
  tr1(g) = timestampof($r.e1)
  trr1 = tr1(g)
  nr=nr + 1
}
loopif $s=slist.e1 passes (0.0,12690.0)
{
  g = group($s) - 20
  inc hitpats(g)
  energys(g) = $s.e1
  inc sectors($s.e1) indexed g
  ts = timestampof($s.e1)
  ts1(g) = timestampof($s.e1)
  tss1 = ts1(g)
  ns=ns + 1
}
td=(ts-tr)+1024
inc timesi(td)
td=(tg-tr)+1024
inc timeg1(td)
td=(tg-ts)+1024
inc timeg2(td)
doloop iii from 1 to 32 step +1
{
  es = energys(iii)
  tss = ts
  nsss = nss(iii)
  if es gt 10
  {
    ss = iii
    es1 = energys(ss)
  }
}
if ns eq 1
{
  nsss = ns
}
doloop ii from 1 to 24 step +1
{
  er = energyr(ii)
  trr = tr
  nrrr = nrr(ii)
  if er gt 10
  {
    rr = ii
    imax = inelas_max(ii)
    imin = inelas_min(ii)
    er1 = energyr(rr)
  }
}
if nr eq 1
{
  nrrr = nr
}
c_si = nr + ns
td = (tss-trr) +1024

!*****_PARTICLE_COINCIDENCE_CONDITION_*****

if td passes (985,1060)
{
  if c_si eq 2
  {
    inc si_mat(es1/4,er1/4)
    ee = ABS(es1-er1)
    inc eeg(ee)
  }
}

!*****_ENERGY_SHARE_CONDITION_*****

if ee lt 1400
{
  inc si_matdc(es1/4,er1/4)
}

!*****_INELASTIC_GATE_CONDITION_*****

if er1 lt imax
{
  if er1 gt imin
  {

!-----_DOPPLER_CORRECTION_-----

ee123 = 0
ecad = 0
ee312 = 0
ecbd = 0
ee321 = 0
eccd = 0

```



```

ee213 = 0
ecdd = 0
doloop i from 1 to 8 step +1
{
!-----TRANSFORMATION_MATRIX_FOR_S3_DETECTOR_CRISTAL_A-----

xb = d_target2s3*sin(sec_phi(ss))*sin(angdis(rr))
yb = d_target2s3*sin(angdis(rr))
zb = d_target2s3*cos(sec_phi(ss))*sin(angdis(rr))
ee123 = energyg1(i)
if ee123 gt 0
{

!-----TRANSFORMATION_MATRIX_FOR_GE_DETECTOR_CRISTAL_A-----

x_1(i)=d_target2ge*sin(crys_a_phi(i))*sin(crys_a_theta(i))
xa = x_1(i)
y_1(i)=d_target2ge*cos(crys_a_theta(i))
ya = y_1(i)
z_1(i)=d_target2ge*cos(crys_a_phi(i))*sin(crys_a_theta(i))
za = z_1(i)
}
caa=(xa*xb+ya*yb+za*zb)/(sqrt(xa*xa+ya*ya+za*za)*sqrt(xb*xb+yb*yb+zb*zb))

!-----ENERGY_DOPPLER_CORRECTED_CRYSTAL_A-----

e11ca(i)=energyg1(i)*(1-beta(rr))*caa/sqrt(1-beta(rr))*beta(rr))
ecad=e11ca(i)
tgg = tg1(i)
trr = tr1(rr)
tss = ts1(ss)
tdgs = (tgg - tss) +1024
tddd = (tgg - trr) +1024

!***** PARTICLE_GAMMA_COINCIDENCE_CONDITION_CRYSTAL_A *****
ngg= nga + ngb + ngc + ngd
if ngg eq 1
{
if tdgs passes (1055,1149)
{
if tddd passes (1055,1149)
{
sumdr(rr)=sumdr(rr)+ecad
sumndr(rr)=sumndr(rr)+ee123
sumnodop(i)=sumnodop(i)+ee123
sumdop(i)=sumdop(i)+ecad
}
}
ee312 = energyg2(i)
if ee312 gt 0
{
x_2(i)=d_target2ge*sin(crys_b_phi(i))*sin(crys_b_theta(i))
xbb = x_2(i)
y_2(i)=d_target2ge*cos(crys_b_theta(i))
ybb = y_2(i)
z_2(i)=d_target2ge*cos(crys_b_phi(i))*sin(crys_b_theta(i))
zbb = z_2(i)
}
cab=(xbb*xb+ybb*yb+zbb*zb)/(sqrt(xbb*xbb+ybb*ybb+zbb*zbb)*sqrt(xb*xb+yb*yb+zb*zb))
e11cb(i)=energyg2(i)*(1-beta(rr))*cab/sqrt(1-beta(rr))*beta(rr))
ecbd=e11cb(i)
tgg = tg2(i)
trr = tr1(rr)
tss = ts1(ss)
tdgs = (tgg - tss) +1024
tddd = (tgg - trr) +1024
if tdgs passes (1055,1149)
{
if tddd passes (1055,1149)
{
sumdr(rr)=sumdr(rr)+ecbd
sumndr(rr)=sumndr(rr)+ee312
sumnodop(i)=sumnodop(i)+ee312
sumdop(i)=sumdop(i)+ecbd
}
}
ee321 = energyg3(i)
if ee321 gt 0
{
x_3(i)=d_target2ge*sin(crys_c_phi(i))*sin(crys_c_theta(i))
xc = x_3(i)
y_3(i)=d_target2ge*cos(crys_c_theta(i))
yc = y_3(i)
z_3(i)=d_target2ge*cos(crys_c_phi(i))*sin(crys_c_theta(i))
zc = z_3(i)
}
cac=(xc*xb+yc*yb+zc*zb)/(sqrt(xc*xc+yc*yc+zc*zc)*sqrt(xb*xb+yb*yb+zb*zb))
e11cc(i)=energyg3(i)*(1-beta(rr))*cac/sqrt(1-beta(rr))*beta(rr))
eccd=e11cc(i)
tgg = tg3(i)
trr = tr1(rr)
tss = ts1(ss)
tdgs = (tgg - tss) +1024
tddd = (tgg - trr) +1024
if tdgs passes (1055,1149)
{
if tddd passes (1055,1149)
{

```


DISC /home/jnorce/Documents/Mavela/PR256E/R62_0
DISC /home/jnorce/Documents/Mavela/PR256E/R60_0
DISC /home/jnorce/Documents/Mavela/PR256E/R59_0
DISC /home/jnorce/Documents/Mavela/PR256E/R58_0
DISC /home/jnorce/Documents/Mavela/PR256E/R57_0
DISC /home/jnorce/Documents/Mavela/PR256E/R56_0
DISC /home/jnorce/Documents/Mavela/PR256E/R55_0
DISC /home/jnorce/Documents/Mavela/PR256E/R54_0
DISC /home/jnorce/Documents/Mavela/PR256E/R53_0
DISC /home/jnorce/Documents/Mavela/PR256E/R52_0
DISC /home/jnorce/Documents/Mavela/PR256E/R51_0
DISC /home/jnorce/Documents/Mavela/PR256E/R50_0
DISC /home/jnorce/Documents/Mavela/PR256E/R49_0
DISC /home/jnorce/Documents/Mavela/PR256E/R48_0
DISC /home/jnorce/Documents/Mavela/PR256E/R47_0
!DISC /home/jnorce/Documents/Mavela/PR256E/R79_0

*finish



Appendix D

GOSIA input

```
OP,FILE
22,3,1
32S1.out
9,3,1
test.f9
8,3,1
test.f8
0,0,0
OP,TITL
32S1 + 194Pt @ 120.3 MeV beam excitation
OP,GOSI
LEVE
1,1,0,0.0
2,1,2,2.2306
3,1,0,3.7784
4,1,2,4.2819
0,0,0,0
ME
2,0,0,0,0
1,2,0.169,-1,1
2,2,-0.05,-1,1
2,3,0.0843884796,-1,1
2,4,0.154397652,0,1
0,0,0,0,0
EXPT
24,16,32
-78,194,120.3,110.59,4,1,0,0,360,0,1 !1
-78,194,120.3,111.15,4,1,0,0,360,0,2 !2
-78,194,120.3,111.73,4,1,0,0,360,0,3 !3
-78,194,120.3,112.34,4,1,0,0,360,0,4 !4
-78,194,120.3,112.97,4,1,0,0,360,0,5 !5
-78,194,120.3,113.66,4,1,0,0,360,0,6 !6
-78,194,120.3,114.38,4,1,0,0,360,0,7 !7
-78,194,120.3,115.15,4,1,0,0,360,0,8 !8
-78,194,120.3,115.96,4,1,0,0,360,0,9 !9
-78,194,120.3,116.81,4,1,0,0,360,0,10 !10
-78,194,120.3,117.73,4,1,0,0,360,0,11 !11
-78,194,120.3,118.70,4,1,0,0,360,0,12 !12
-78,194,120.3,119.73,4,1,0,0,360,0,13 !13
-78,194,120.3,120.84,4,1,0,0,360,0,14 !14
-78,194,120.3,122.02,4,1,0,0,360,0,15 !15
-78,194,120.3,123.28,4,1,0,0,360,0,16 !16
-78,194,120.3,124.64,4,1,0,0,360,0,17 !17
-78,194,120.3,126.09,4,1,0,0,360,0,18 !18
-78,194,120.3,127.66,4,1,0,0,360,0,19 !19
-78,194,120.3,129.34,4,1,0,0,360,0,20 !20
-78,194,120.3,131.15,4,1,0,0,360,0,21 !21
-78,194,120.3,133.04,4,1,0,0,360,0,22 !22
-78,194,120.3,135.22,4,1,0,0,360,0,23 !23
-78,194,120.3,137.49,4,1,0,0,360,0,24 !24
CDNT
SPL,1.
INT,24.
1,1000
2,1000
3,1000
4,1000
5,1000
6,1000
7,1000
8,1000
9,1000
10,1000
11,1000
12,1000
13,1000
14,1000
15,1000
16,1000
```




```

10,10
4           !18
113.85,116.05,118.26,120.46
5.738,5.707,5.675,5.644
10,10
4           !19
113.85,116.05,118.26,120.46
5.738,5.707,5.675,5.644
10,10
4           !20
113.85,116.05,118.26,120.46
5.738,5.707,5.675,5.644
10,10
4           !21
113.85,116.05,118.26,120.46
5.738,5.707,5.675,5.644
10,10
4           !22
113.85,116.05,118.26,120.46
5.738,5.707,5.675,5.644
10,10
4           !23
113.85,116.05,118.26,120.46
5.738,5.707,5.675,5.644
10,10
4           !24
113.85,116.05,118.26,120.46
5.738,5.707,5.675,5.644
10,10
UP,EXIT}

```



Bibliography

- [1] S. M. Wong, *Introductory Nuclear Physics*, 1st Ed., Prentice-Hall, 192 (1990).
- [2] K. S. Krane, *Introductory Nuclear Physics*, 1st Ed., John Wiley and Sons, 136 (1988).
- [3] <http://www.nndc.bnl.gov/masses/mass.mas03>
- [4] D. J. Rowe and J Wood, *Fundamentals of Nuclear Models: Foundational Models*, 1st Ed, World Scientific Publishing Co. Pte. Ltd, (2010).
- [5] D. J. Griffiths, *Introduction to Quantum Mechanics*, 2nd Ed., Prentice Hall, 181-183 (2005).
- [6] K. S. Krane, *Introductory Nuclear Physics*, 1st Ed., John Wiley and Sons, 134 (1988).
- [7] D. J. Griffiths, *Introduction to Quantum Mechanics*, 1st Ed., Prentice-Hall, 221-222 (1994).
- [8] K. Alder and A. Winther, *Electromagnetic excitation*, North-Holland, Amsterdam, (1975).
- [9] O. Häusser, *Nuclear spectroscopy and reactions C*, ed. J. Cerny, Academy Press, New York, 55 (1974).
- [10] <https://en.wikipedia.org/wiki/Spheroid/media/File:Ellipsoid-rot-ax.svg>
- [11] R. H. Spear, *Phys. Rep.* **73**, 369-390 (1981).
- [12] K. Nakai, J. L. Quebert, F. S. Stephens and R. M. Diamond, *Phys. Rev. Lett.* **24**, 903 (1970).
- [13] W. J. Vermeer, M. T. Esat, R. H. Spear, *Nucl. Phys. A* **389**, 185-190 (1982).
- [14] O. Häusser, T. K. Alexander, A. B. McDonald and W. T. Diamond, *Nucl. Phys. A* **175**, 593-605 (1971).
- [15] A. Olin *et al*, *Nucl. Phys. A* **221**, 555-563 (1974).
- [16] D. Schwalm, E. K. Warburton, *Nucl. Phys. A* **293**, 425-480 (1977).
- [17] G. C. Ball, O. Häusser, T. K. Alexander, W. G. Davies, J. S. Forster, I. V. Mitchell, J. R. Beene and D. Horn, *Nucl. Phys. A* **349**, 271-284 (1980).

- [18] G. Dannhäuser, J. de Boer, R. Lutter and F. Reiss, *Z. Phys. A, Atoms and Nuclei* **300**, 71-75 (1981).
- [19] D. C. Kean, in: *Nuclear Interactions*, ed. B. A. Robson, *Lecture Notes in Physics* **92**, Springer-Verlag, Berlin, 80 (1978).
- [20] R. H. Spear, T. H. Zabel and D. C. Kean, *Phys. Lett. B* **76**, 559 (1978).
- [21] W. J. Vermeer, M. T. Esat, M. P. Fewell, R. H. Spear, A. M. Baxter and S. M. Burnett, *Phys. Lett. B* **138**, 365 (1984).
- [22] K. H. Speidel, S. Scheilke, J. Leske, P. Maier-Komor, S. J. Q. Robinson, Y. Y. Sharon and L. Zamick, *Phys. Lett. B* **632**, 207-211 (2006).
- [23] T.A. Chubb, *Condensed Matter Nuclear Science*, **2**, 51-59 (2009).
- [24] K. Alder, A. Bohr, T. Huus, B. Mottelson and A. Winther, *Study of Nuclear Structure by Electromagnetic Excitation with Accelerated Ions*, *Reviews of Modern Physics*, **28**, 437 (1956).
- [25] R. H. Spear, *Physics Reports* **73**, 369-390 (1981).
- [26] R. H. Spear, T. H. Zabel and D. C. Kean, *Phys. Lett. B* **76**, 559 (1978).
- [27] F. K. McGowan, P. H. Stelson, *Coulomb Excitation, Nuclear Spectroscopy and Reactions, Part C*, 5 (1974).
- [28] <http://hyperphysics.phy-astr.gsu.edu/hbasees/Nuclear/rutsca3.html>.
- [29] D. Cline, *Gosia User Manual for Simulations and Analysis of Coulomb Excitation Experiments*, 17 (2012)
- [30] F. K. McGowan, P. H. Stelson, *Coulomb Excitation, Nuclear Spectroscopy and Reactions, Part C*, 8-9 (1974).
- [31] K. S. Krane, *Introductory Nuclear Physics*, 1st Ed., John Wiley and Sons, (1988).
- [32] F. K. McGowan, P. H. Stelson, *Nuclear Spectroscopy and Reactions, Part C*, 15 (1974).
- [33] J. de Boer, J. Eichler, *The Reorientation Effect*, *Advances in Nuclear Physics*, **1**, 8 (1968).
- [34] K. Alder, A. Bohr, T. Huus, B. Mottelson and A. Winther, *Study of Nuclear Structure by Electromagnetic Excitation with Accelerated Ions*, *Reviews of Modern Physics*, **28**, 436 (1956).
- [35] K. S. Krane, *Introductory Nuclear Physics*, 1st Ed., John Wiley and Sons, Vol. **1**, 117 (1988).
- [36] J. Lilley, *Nuclear Physics principles and applications*, 1st Ed., John Wiley and Sons, 41 (2001).
- [37] J. Lilley, *Nuclear Physics principles and applications*, 1st Ed., John Wiley and Sons, 45 (2001).

- [38] S. S. M. Wong, *Introductory Nuclear Physics*, 2nd Ed., Wiley-VCH, 235 (2004).
- [39] MIT Nuclear Structure Lecture Notes, <https://ocw.mit.edu/courses/nuclear-engineering/>.
- [40] R. R. Roy *et al*, *Nuclear Physics*, 1st Ed., John Wiley and Sons, 234 (1967).
- [41] K. S. Krane, *Introductory Nuclear Physics*, 1st Ed., John Wiley and Sons, 131 (1988).
- [42] A. Bohr *et al*, *Nuclear Structure*, Vol. 1, World Scientific, 332 (1998).
- [43] K. S. Krane, *Introductory Nuclear Physics*, 1st Ed., John Wiley and Sons, 34 (1988).
- [44] D. Cline, T. Czonyk, A. B. Hayes, P. Napiorkowski, N. Warr and C. Y. Wu, *Gosia User Manual for Simulation and Analysis of Coulomb Excitation Experiments*, (2012).
- [45] <http://www.physics-and-radio-electronics.com/electronic-devices-and-circuits/semiconductor-diodes/reversebiaseddiode.html>
- [46] G. F. Knoll, *Radiation Detection and Measurements*, 3rd Edition, John Wiley and Sons Inc., 29 (2000).
- [47] S. N. Ahmed, *Physics and Engineering of Radiation Detection*, 1st Edition, 77 (2007).
- [48] <http://www.europeanmedical.info/emission-tomography/interaction-of-photons-with-matter.html>
- [49] <http://drgstoothpix.com/2012/10/24/attenuation-compton-scatter/>
- [50] <http://www.chegg.com/homework-help/questions-and-answers/pair-production-photon-converted-electron-positron-positron-rest-mass-512-kev-electron-pos-q7108095>
- [51] <https://sites.google.com/a/hartdistrict.org/ms-smith/home/modern-solid-materials/chapter-21-metallurgy-and-the-chemistry-of-metals/21-3-band-theory-of-electrical-conductivity>
- [52] <https://sites.google.com/a/hartdistrict.org/ms-smith/home/modern-solid-materials/chapter-21-metallurgy-and-the-chemistry-of-metals/21-3-band-theory-of-electrical-conductivity>.
- [53] <http://www.canberra.com/products/detectors/pdf/Clover-Detector-C39840.pdf>.
- [54] N. A. Khumalo, *Study of two octupole vibrations in ^{146}Gd* , MSc (2013).
- [55] <https://www.lnl.infn.it/prisma/claratechnical/node3.html>.
- [56] C. Mehl, *Developing sorting for Coulomb excitation experiment*, MSc (2016).

- [57] [cite=http://www.mesytec.com/products/datasheets/MPR-16.pdf](http://www.mesytec.com/products/datasheets/MPR-16.pdf).
- [58] <https://web-docs.gsi.de/wolle/EBatGSI/STOPPEDBEAMS/ACTIVESTOPPER/DOCUMENTS/MH4V13.pdf>.
- [59] G. F. Knoll, Radiation Detection and Measurement, 3rd Ed., 2000, John Wiley and Sons Inc., 116 (2000).
- [60] <https://arxiv.org/pdf/1506.04633.pdf>
- [61] <http://www.nndc.bnl.gov/be2/adopted.jsp>
- [62] M. Bender, H. Flocard, and P. -H. Heenen, Phys. Rev. C **68**, 044321 (2003).
- [63] D. J. Rowe, Nuclear Collective Motion (1970).
- [64] K. Heyde and J. L. Wood, Rev. Mod. Phys. **83**, 1467 (2011).

